6. CONFINEMENT AND TRANSPORT

This chapter is the basis for our expectation that QPS will be able to obtain the plasma parameters needed to achieve its physics objectives. The expected plasma performance is based on 0-D projections from the standard stellarator confinement scaling; 1-D calculations of plasma profiles; and neoclassical thermal confinement calculations including single particle orbits, the effect of electric fields, and Monte Carlo transport calculations.

6.1. 0-D Plasma Parameter Projections

A large database exists for stellarators with aspect ratios R/a > 5. In 1995 a collection of data sets from the world stellarators was used to obtain a common scaling relation that was the best fit to the data. The global energy confinement time τ_E from these data sets is plotted in Figure 6.1 against this so-called "ISS95" scaling relation, $\tau_E^{ISS95} = 0.079 a_p^{2.21} R^{0.65} P^{-0.59} n^{0.51} B^{0.83} \iota^{-0.4}$ with R and a_p in m, B in T, n in 10^{19} m^{-3}, and P in MW. W 7-AS and LHD have achieved energy confinement times up to 2.5 times the τ_E^{ISS95} value. The confinement improvement is attributed by these groups to the low shear in W 7-AS and the large plasma radius in LHD. QPS has both these attributes, but there is no comparable data for comparison at the low aspect ratio of QPS, a factor of 2-4 below those of the experiments plotted in Figure 6.1. One of the objectives of QPS is to determine the scaling of anomalous transport at very low aspect ratios and its connection with that for the larger aspect ratio stellarators.

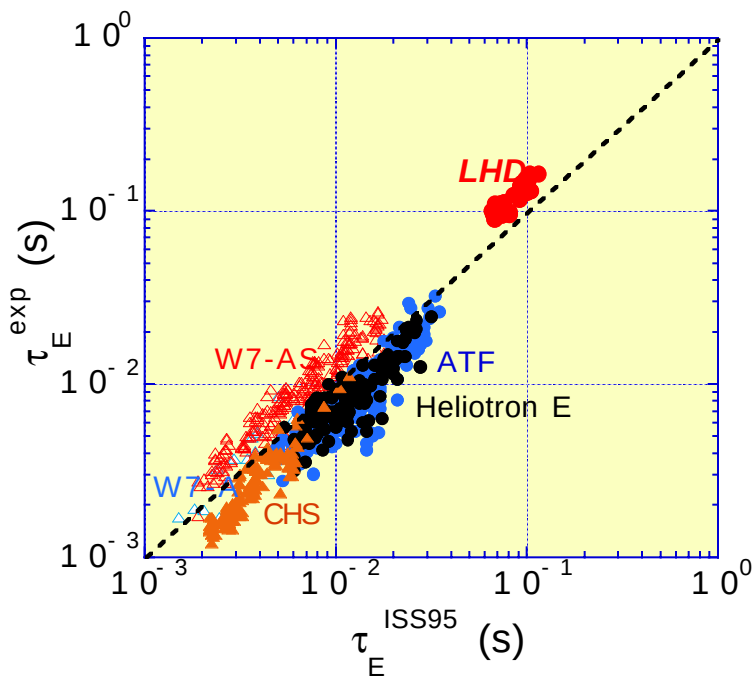

Figure 6.1. The experimental basis for the ISS95 stellarator confinement scaling relation.

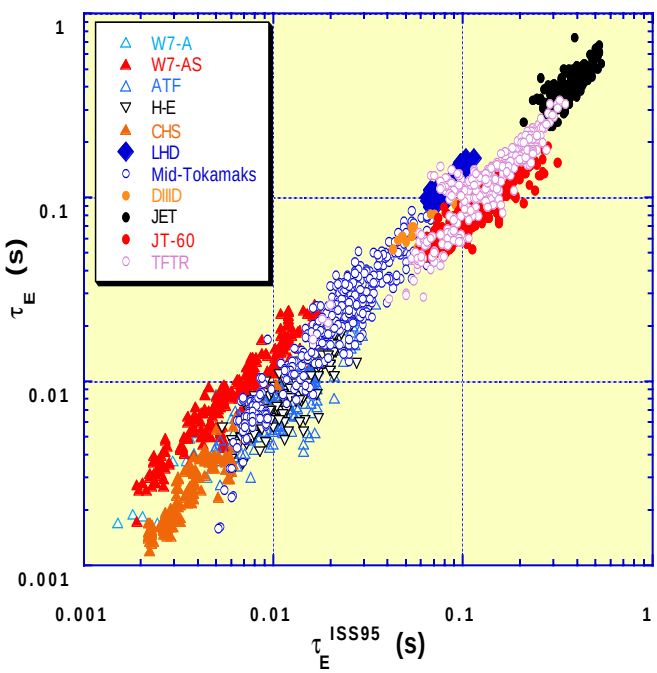

Figure 6.2. The combined stellarator and tokamak L-mode databases.

This same confinement scaling fits the L-mode database, as shown in Figure 6.2. This gives some confidence in the generality of this expression.

The ISS95 confinement scaling can be used to project QPS performance for various assumed values of the density *n*, magnetic field strength B, and confinement improvement factor H-ISS95 = τ_E/τ_E^{ISS95}. Figure 6.3 shows contours of $\langle\beta\rangle$/H-ISS95 in the experimentally relevant *P* vs. *n* plane. The loci of the Sudo density "limit", $n_{Sudo}(10^{20}\ m^{-3}) = 0.25[P(MW)B(T)/\{R(m)a(m)^2\}]^{1/2}$, obtained from Heliotron-E data and 1.5 times that value are also indicated. However, this is not really a density limit, just the value of density above which the stored energy peaked with increasing density in Heliotron E. Density values higher than indicated by this scaling are routinely obtained in stellarators: a factor of 1.2 higher was obtained in the ATF experiments and values between 1 and 2 higher are obtained in LHD experiments. In fact the best performance in LHD is obtained for $n = 2n_{Sudo}$. The dots in Figure 6.3 indicate values of density and power used in the 1-D transport calculations in the next section and the squares indicate values used in the neoclassical transport calculations in the following section. The Sudo density value and a value of 1.5 for H-ISS95 are assumed in the estimates of the QPS plasma parameters. For these assumptions, the contours in Figures 6.3 and 6.4 range in $\langle\beta\rangle$ from 0.75% to 3%, in τ_E from 5 ms to 20 ms, and in <T>, the density average of the electron and ion temperatures, from 0.3 keV to 0.9 keV.

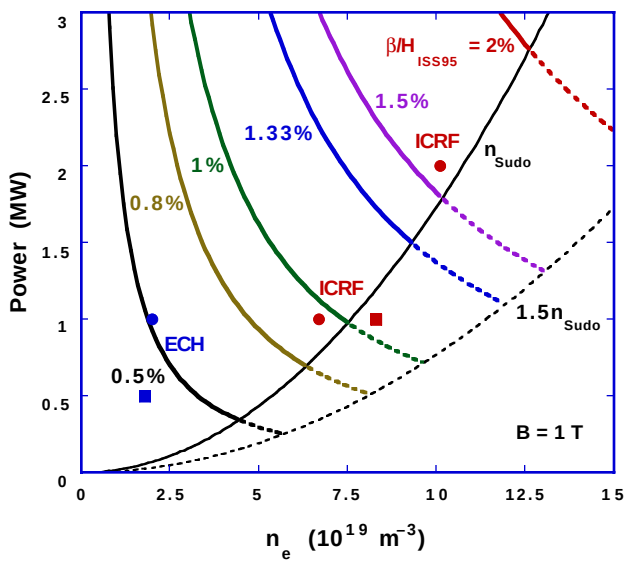

Figure 6.3. Contours of constant ⟨β⟩/H-ISS95 in the *P* vs. *n* plane for B = 1 T.

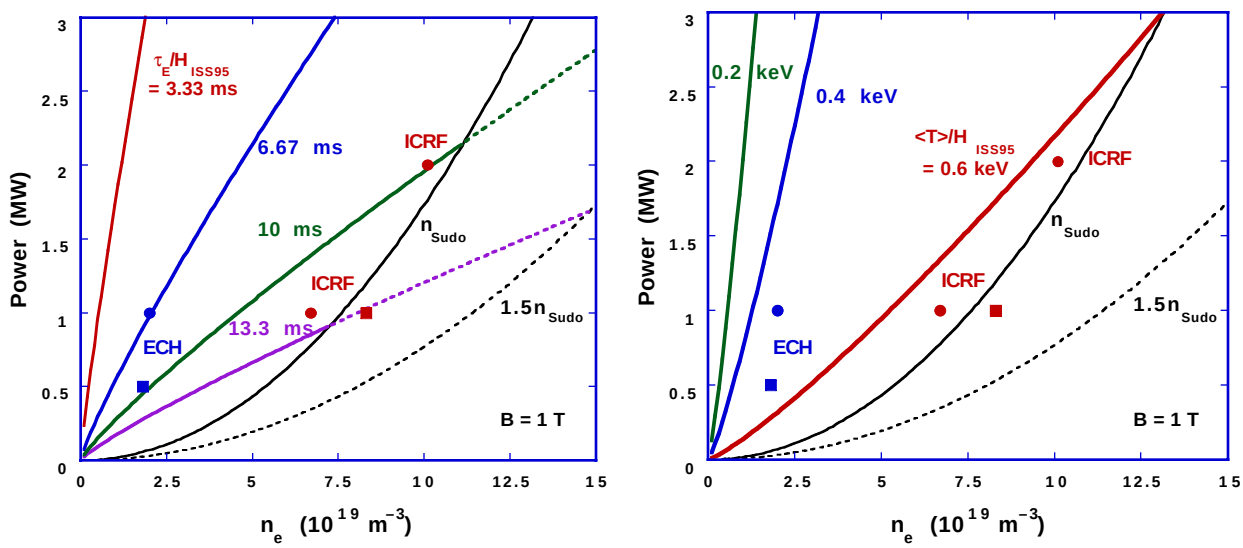

Figure 6.4. Contours of constant τ_E/H-ISS95 (left) and constant <T>/H-ISS95 in the *P* vs. *n* plane for B = 1 T.

6.2. 1-D Plasma Parameter Projections

The profile analysis used in the NCSX study was also applied to QPS. The calculations involve three steps:

- estimating the E_r necessary for ambipolar particle flux,
- estimating the ripple transport, and
- calculating the temperature profiles.

The temperature profile calculations are solutions of the coupled power balance equations for the electron and ion temperatures. The thermal diffusivities have two components: neoclassical ripple transport and an anomalous transport model with an adjustable multiplier. The ripple transport depends on the density and temperature profiles – and their gradients - as well as the radial electric field which, in turn, is established by requiring the helical particle transport to be ambipolar. Consequently, all parameters must be solved for simultaneously, so an iterative procedure is used until the temperatures and transport fluxes have converged. By construction, the algorithm for finding the ambipolar electric field searches for the ion root at the edge of the plasma. The Shaing-Houlberg analytic model used for neoclassical helical transport is based on a single-helicity magnetic configuration in which the effective helical ripple calculated by the NEO code [R] is used for all transport regimes. This procedure is justified by: 1) a successful NCSX benchmark with the GTC code, which makes no assumption concerning the collisionality regime, and 2) through the ambipolar E_r the electrons effectively set the overall level of transport and they are in the $1/\nu$ regime. The effective helical ripple for QPS configurations is shown in Figure 6.19(a).

The ripple transport is the low-collisionality non-symmetric component of the transport. It is an upper bound which will exist only before superbanana effects drive the transport back down at low enough collisionalities. The neoclassical axisymmetric (Chang-Hinton) transport used in the NCSX studies is not relevant for QPS because for quasi-poloidal symmetry the symmetric component of transport can be quite low as a result of the short toroidal extent and narrow radial thickness of the banana orbits. For quasi-toroidally-symmetric devices the symmetric component of transport can be much higher [R] than the ripple component ($\sim \varepsilon_{eff}^{3/2}$) computed here at moderately low collisionalities.

The anomalous diffusivity is adjusted in the calculations to match a target $\langle\beta\rangle$ or H-ISS95 value. The power conducted by the anomalous term can then be compared to the neoclassical conduction power as a measure of the confinement margin. Usually a simple spatially-uniform anomalous transport model based on ISS95 confinement scaling is used with a confinement multiplier H-ISS95 = 1.5. The same multiplier is used for both the electron and ion diffusivities. Values of 2.4-2.5 have been obtained in W 7-AS and LHD, so the value used here might be conservative. Achieving a value for H-ISS95 of 1.5, or higher, would be a minimum objective of the QPS experiments.

The power balance equations are solved with an assumed density profile shape, and assumed outer boundary temperatures. Broad density profiles are typically observed in stellarators and RF power deposition profiles are peaked on axis. The density and power deposition profiles used here are shown in Figure 6.5. The heating power is initially split between ions and electrons in the ratio 20%:80% for the high density ICRF and EBW heating case and 0:100% for the low-density ECH case. Coulomb collisional transfer between electrons and ions redistributes the power between the two species.

Figure 6.6 shows the calculated ambipolar electric field and temperature profiles for an ICRF/EBW case with P = 2 MW at B = 1 T. The $n^{0.51}$ density dependence of the ISS-95 scaling favors

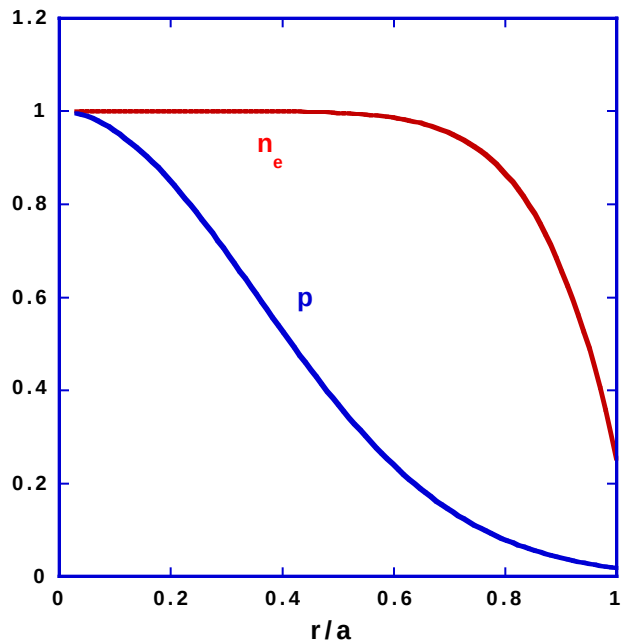

Figure 6.5. density and power deposition profiles for the QPS cases.

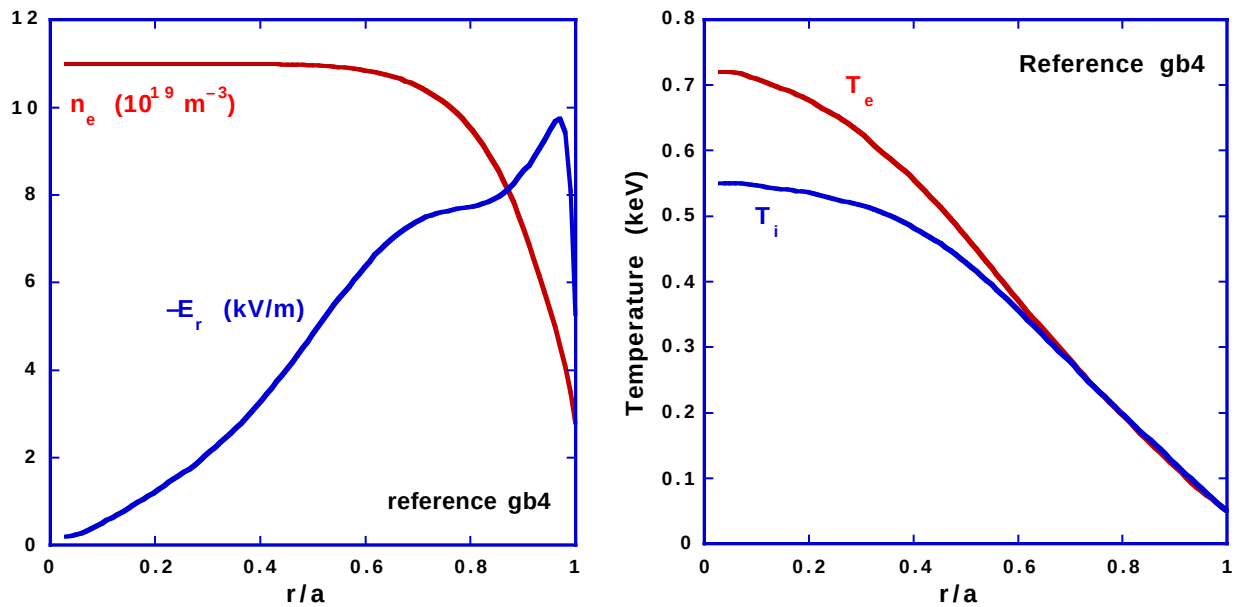

Figure 6.6. (a) Assumed density profile and calculated radial ambipolar electric field, and (b) calculated electron and ion temperature profiles for the reference gb4 configuration for $n_e = 10^{20}$ m^{-3} and $P_{ICRF} = 2$ MW at B = 1 T.

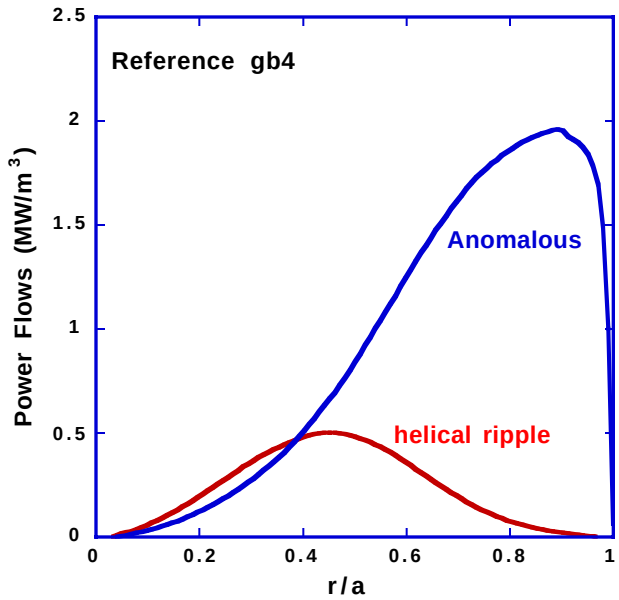

Figure 6.7. Power loss channels for the reference gb4 configuration for $n_e = 10^{20}$ m^{-3} and $P_{ICRF} = 2$ MW at B = 1 T.

operation at high density for obtaining higher values of the confinement time τ_E and $\langle\beta\rangle$. The line-average density is 10^{20} m^{-3}, slightly lower than the Sudo density "limit" for this case, n = 1.06 x 10^{20} m^{-3}. The radial electric field is in the "ion root" regime everywhere in the plasma, as observed in stellarator experiments at higher densities. The ripple-induced transport is comparable with anomalous transport out to r/a = 0.4 in Figure 6.7, but becomes much smaller than the anomalous transport in the outer 5/6 of the plasma volume. The H-ISS95 confinement multiplier used here (H-ISS95 = 1.5) gives $\langle\beta\rangle$ = 2.32%, so there is some margin for enhanced anomalous transport or neoclassical transport while still being able to obtain $\langle\beta\rangle$ = 2%. Targeting $\langle\beta\rangle$ = 2% requires only an H-ISS95 multiplier of 1.29. While initially 80% of the power is assumed to go to the electrons, the ion temperature is comparable with the electron temperature because the neoclassical losses are larger in the electron channel and there is sufficient energy transferred at these densities.

Table 6.1 lists the parameters obtained with ICRF/EBW heating for different values of B and heating power for the reference gb4 configuration and two lower-ripple variants, gb5_12d and gb5_12c. The ripple-induced component of the transport is even smaller in these configurations. Operation at B = 0.5 T gives slightly higher values of $\langle\beta\rangle$, ≈2.8%, for all three configurations, but with lower values of plasma density, temperature, and confinement time. The confinement multiplier required for a value of $\langle\beta\rangle$ = 2% is H-ISS95 ≈1.06.

Ripple-induced transport can be enhanced by operation at lower density. Ripple transport is more important at the higher temperatures obtained at lower densities because it has a strong temperature dependence. Figure 6.8 shows the calculated ambipolar electric field and temperature profiles for an ECH case with P = 1 MW at B = 1 T. The line-average density is 2 x 10^{19} m^{-3}, consistent with second-harmonic 28-GHz X-mode or 53.2-GHz O-mode operation. Density values higher than

Table 6.1. Calculated plasma parameters for the reference QPS configuration and variants with lower-ripple for ICRF/EBW-heated cases.

Case	B T	P MW	n_e, n_{Sudo} 10^{19} m^{-3}	T_e keV	T_i keV	τ_E ms	$-E_{r,max}$ kV/m	$\langle\beta\rangle$ %
gb4	0.5	1	5.0, 5.3	0.43	0.31	9.0	5.9	2.77
	1	1	6.7, 7.5	0.64	0.48	18.3	10.0	1.41
	1	2	10.1, 10.6	0.72	0.55	15.1	10.8	2.32
gb5_12d	0.5	1	5.0, 5.3	0.47	0.36	9.1	5.7	2.82
	1	1	6.7, 7.5	0.72	0.56	18.8	9.3	1.44
	1	2	10.1, 10.6	0.80	0.64	15.5	10.2	2.38
gb5_12c	0.5	1	5.0, 5.3	0.48	0.37	9.1	5.7	2.81
	1	1	6.7, 7.5	0.76	0.61	18.9	9.2	1.46
	1	2	10.1, 10.6	0.83	0.67	15.4	9.9	2.38

the cutoff density were obtained in Heliotron-DR at high power density. The radial electric field is in the "electron root" regime out to r/a = 0.9. The electron temperature is much larger than the ion temperature because all the ECH power goes initially to the electrons and the only power to the ions is from collision transfer, which is small at this low density. The ripple-induced transport dominates out to r/a = 0.85 in Figure 6.9. The H-ISS95 = 1.5 confinement multiplier assumed here gives $\langle\beta\rangle$ = 0.77%.

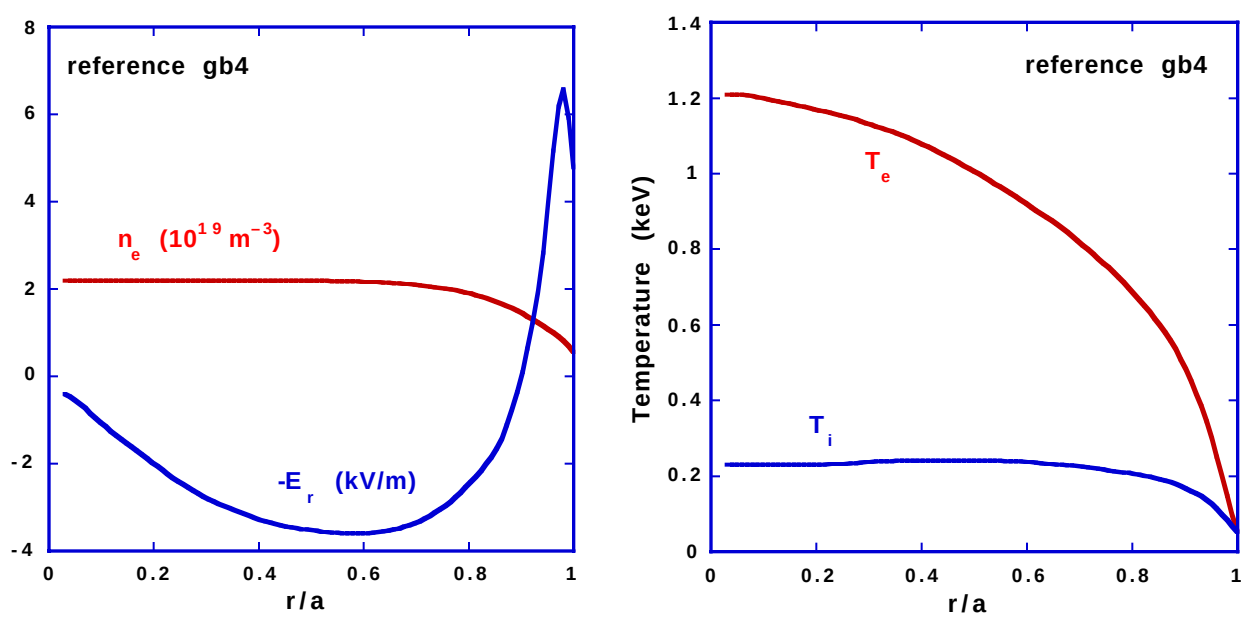

Figure 6.8. (a) Assumed density profile and calculated radial ambipolar electric field, and (b) calculated electron and ion temperature profiles for the reference gb4 configuration for $n_e = 2 \times 10^{19}$ m^{-3} and P_{ECH} = 1 MW at B = 1 T.

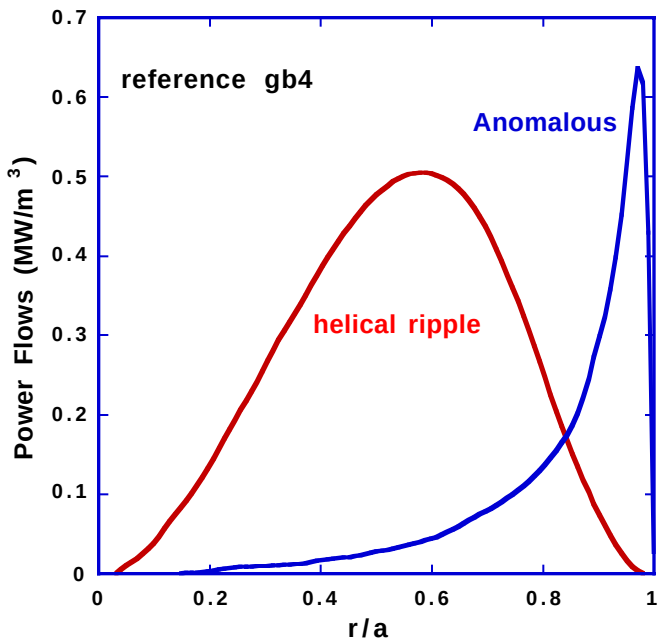

Figure 6.9. Power loss channels for the reference gb4 configuration for $n_e = 2 \times 10^{19}$ m^{-3} and $P_{ECH} = 1$ MW at B = 1 T.

Table 6.2 lists the parameters obtained with ECH heating for two values of B at 1-MW heating power for the reference gb4 configuration and two lower-ripple variants, gb5_12d and gb5_12c. The ripple-induced component of the transport is smaller in these configurations. Operation at B = 0.5 T gives slightly higher values of $\langle\beta\rangle$, ≈ 0.87%, for all three configurations, but with lower values of plasma density, temperature, and confinement time. The effect of lowering the ripple is illustrated in Figures 6.10 and 6.11. The ripple-induced transport is dominant only in the central 20% of the plasma volume (out to r/a = 0.45) in Figure 6.10 vs. the central 70% of the plasma volume (out to r/a = 0.85) in Figure 6.9. The electric field becomes stronger in the mid region of the plasma as the ripple is reduced, as shown in Figure 6.11. The ambipolar potential

Table 6.2. Calculated plasma parameters for the reference QPS configuration and variants with lower-ripple for ECH cases.

Case	B T	n_e 10^{19} m^{-3}	T_e keV	T_i keV	τ_E ms	$-E_r$ kV/m	$\langle\beta\rangle$ %
gb4	0.5	0.5	1.52	0.11	2.8	–39.1	0.86
	1	2.0	1.21	0.23	10.0	–3.6	0.77
gb5_12d	0.5	0.5	1.98	0.11	2.8	–24.5	0.87
	1	2.0	1.48	0.29	10.2	–7.4	0.79
gb5_12c	0.5	0.5	2.30	0.11	2.9	–21.1	0.88
	1	2.0	1.68	0.33	10.1	–11.5	0.78

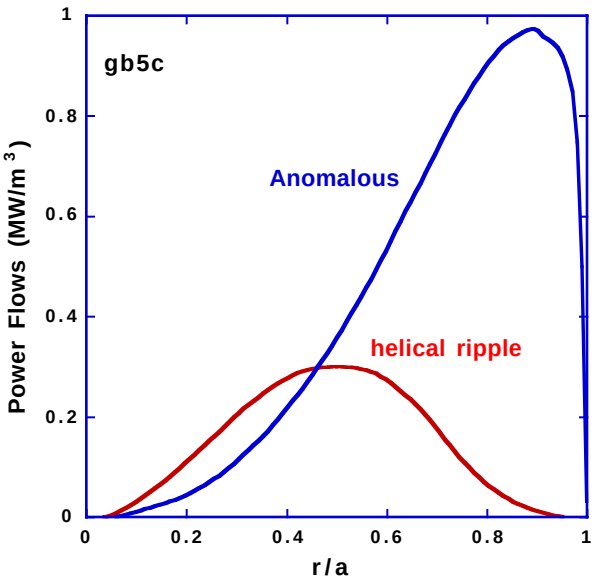

Figure 6.10. Power loss channels for the reference gb5c configuration for $n_e = 2 \times 10^{19}$ m^{-3} and $P_{ECH} = 1$ MW at B = 1 T.

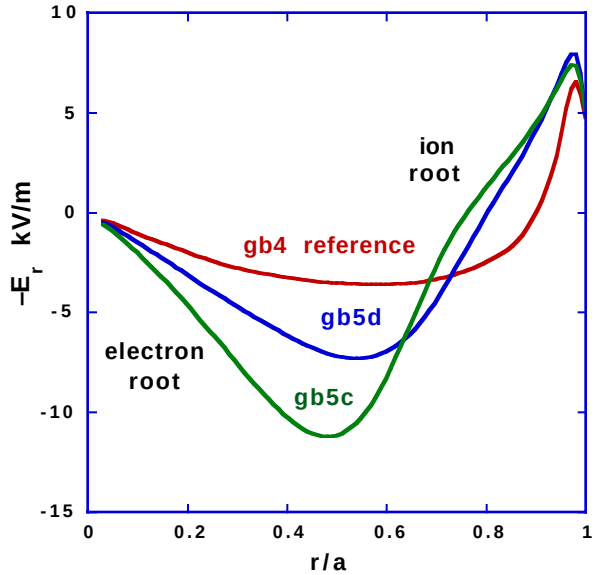

Figure 6.11. Increase of the ambipolar electric field with decreasing ripple.

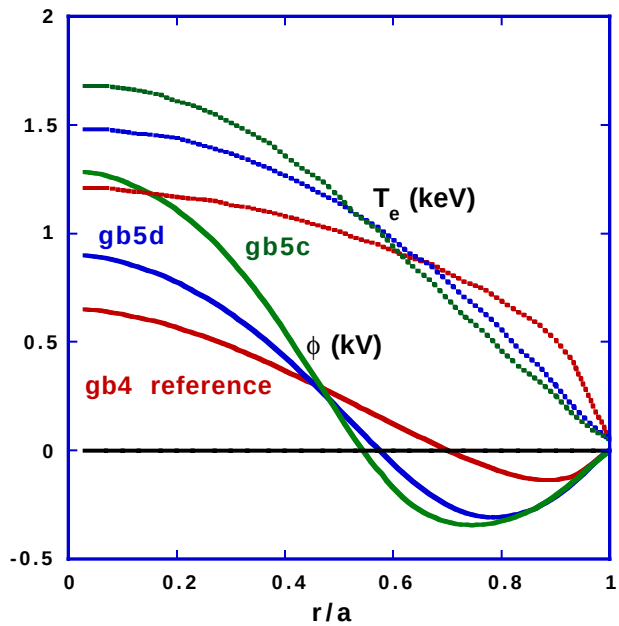

Figure 6.12. The ambipolar potential is more peaked and the value is comparable to T_e for the three QPS cases with different ripple.

is more peaked than the electron temperature profile but is comparable in magnitude, as shown in Figure 6.12.

6.3. Neoclassical Thermal Confinement

The achievement of acceptable levels of neoclassical confinement has guided our QPS design optimization efforts since the beginning of this project.[1,2,3,4,5] The goal of this design has been to develop a compact configuration in which neoclassical confinement times exceed the anomalous stellarator ISS95 scaling law by a significant factor (5 - 10). The rationale behind this target has been to allow sufficient separation between neoclassical and anomalous levels so that noticeable changes in confinement would be observable when (and if) this experiment accesses enhanced confinement (i.e., turbulence suppression) regimes. Such regimes are now observed on most existing stellarators and exploration of their mechanisms and thresholds in the presence of quasi-poloidal symmetry is expected to form an important goal for a QPS experiment. The expected neoclassical thermal confinement properties of our reference configuration have been evaluated for a variety of operational regimes that can be accessed using the ECRH and ICRH heating sources that are anticipated to be available for QPS. Table 6.3 lists plasma parameters that are projected, based on different magnetic field strengths, different heating power levels at several frequencies, and using ISS95 scaling. In the following, we focus on the B = 1 T cases for the transport studies of the QPS device.

TABLE 6.3. - PLASMA PARAMETERS FOR A <B> = 0.5 TO 1 T, N_{fp} = 2, DEVICE, BASED ON ISS95 SCALING WITH ENHANCEMENT FACTOR H = 1.

Heating/ Magnetic field	Density ($X^{\circ}10^{20\circ}m^{-3}$)	T_e, T_i (keV)	ν_{*e}, ν_{*i}	<β>
0.5 MW ECH B°=°1 T	0.18	1.4, 0.15	0.02, 1.6	0.7%
1 MW ECH B°=°0.5 T	0.045	2.1, 0.2	0.002, 0.22	1%
1 MW ICH B°=°1 T	0.83	0.5, 0.5	0.68, 0.64	2%
1 MW ICH B°=°0.5 T	0.59	0.4, 0.25	0.75, 1.8	3.7%

These parameters are based on ISS95 scaling for an earlier R_0 = 0.83 m device, for the indicated levels of heating power and magnetic field strength, but are close to those that characterize the current reference device. Since the more recent reference configuration will sample parameters close to these, they will be used as test cases for our current design. As can be seen, a significant range of collisionality is covered by ECH and ICH heating scenarios. As will be shown below, this will allow tests of transport in both $D \sim 1/\nu$ and $\sim \nu^{1/2}$ regimes; also, for the ECH cases plasma energy losses will generally be dominated by electrons (which will be in the $1/\nu$ regime) while for ICH cases losses will be dominated by ions. The tools used to evaluate confinement in QPS configurations include single particle orbit trajectories, J adiabatic invariant contours[6], the NEO code[7], the DKES[11,12] drift kinetic solver, and the DELTA5D[8] Monte Carlo code. In addition, DELTA5D has been benchmarked for one of our earlier quasi-helical configurations against the

GTC[9] gyrokinetic particle simulation code. In the following sections we describe these tools in more detail and present results obtained with them for the QPS reference configuration (GB4).

6.2.1. Single Particle Orbits

As discussed above, the reference configuration (GB4) exhibits approximate poloidal symmetry in its |B| spectrum for radii far enough from the plasma edge (see Figures 3.10-11 in Chapter 3). The fact that poloidal symmetry cannot be achieved precisely, leads to some level of direct orbit loss. For particles trapped in the local magnetic wells, this loss occurs via a gradual outward drift over many bounces. In Figure 6.13 we show the variation of |B| along a magnetic field line (going about 6 transits around the torus) for an inner and outer flux surface. For regions near the magnetic axis, the ripple remains finite and the wells in |B| are relatively symmetric. Here a relatively simple distinction between trapped and untrapped orbits is possible and there is only a single dominant well structure in |B|. Near the outer flux surface regions, multiple trapping regions are present, leading to possibilities for collisionless trapping and de-trapping near the transitional boundaries in pitch angle space between trapped and passing orbits.

(a)

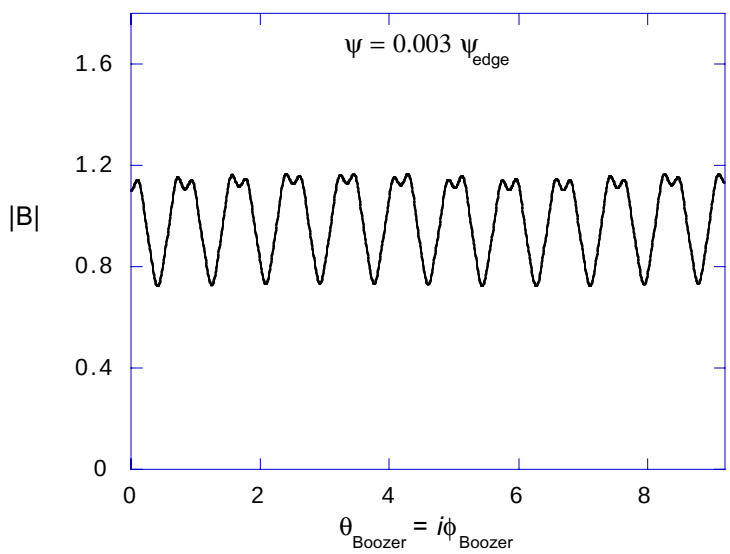

(b)

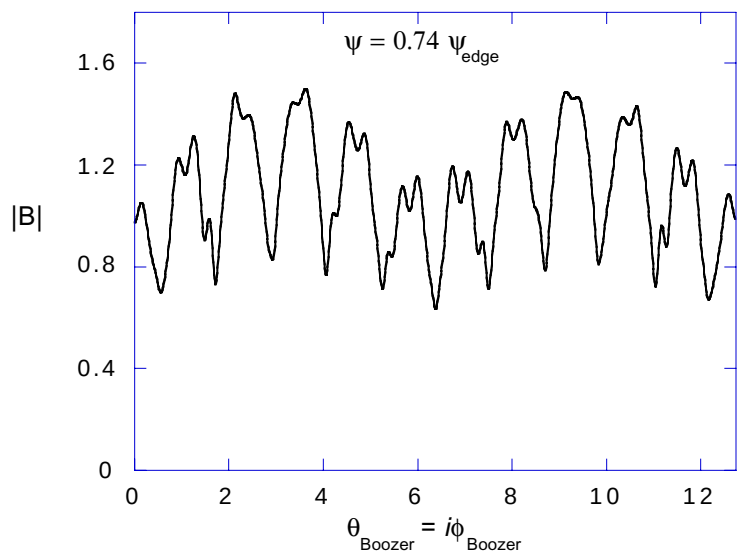

Figure 6.13 Variation of |B| along a field line for (a) $\psi/\psi_{edge} = 0.003$, (b) $\psi/\psi_{edge} = 0.75$.

For passing and transitional particles direct losses can also arise from the presence of drift surface islands and regions of stochasticity which manifest themselves over many toroidal transits. The size of these islands is a function of the particle energy, with this type of loss most important for more energetic ions. Also, both of these types of losses can be relatively slow due to the fact that the (approximately) poloidally symmetric magnetic structure more nearly aligns **B** and $\nabla|\mathbf{B}|$ and thus minimizes the **B** x $\nabla|\mathbf{B}|$ drift component normal to the magnetic surface to a greater degree than is possible with other types of stellarator symmetry. Finally, the effects of this direct loss are minimized, at least for thermal particles, by the influence of the ambipolar electric field and by finite collisionality.

A typical direct orbit loss for a deeply trapped ion in our reference configuration is illustrated in Figure 6.14(a). Figure 6.14(b) plots equivalent orbits in the ATF torsatron (which was not designed to be close to any form of quasi-symmetry) for comparison. For the case shown in Figure 6.14(a) the bounce motion occurs within a single field period. As mentioned above, more complex orbital motion can also occur near trapped-passing transitional regions where orbits can be trapped over a few bounces, become passing as they drift and then become trapped again. Some of the orbits plotted in Figure 6.14(b) for the ATF device have this latter characteristic Figure 6.14(a) shows, however, that the equivalent trapped orbit in the reference configuration with no electric field (the blue orbit) takes many more bounces to leave the confined volume than for a torsatron such as ATF [Figure 6.14(b)]. In real time, the reference configuration orbit remained within the confined volume for 4-5 times longer than the equivalent orbit in ATF. This slower radial drift is directly related to the closer alignment of **B** and $\nabla|\mathbf{B}|$ in the QPS configuration, as mentioned earlier. The other consequence of the slower radial drift which is illustrated in Figure 6.14(a) is the degree with which orbits can become confined in the presence of small components of radial electric field. Even with

$e\phi(a)/\varepsilon = 0.1$ (ε is the particle energy) the orbits close poloidally and are therefore confined. Although this level of electric field provides some degree of confinement of the ATF orbit (red curve) the orbit remains rather pathological and experiences multiple trapping/detrapping transitions.

(a)

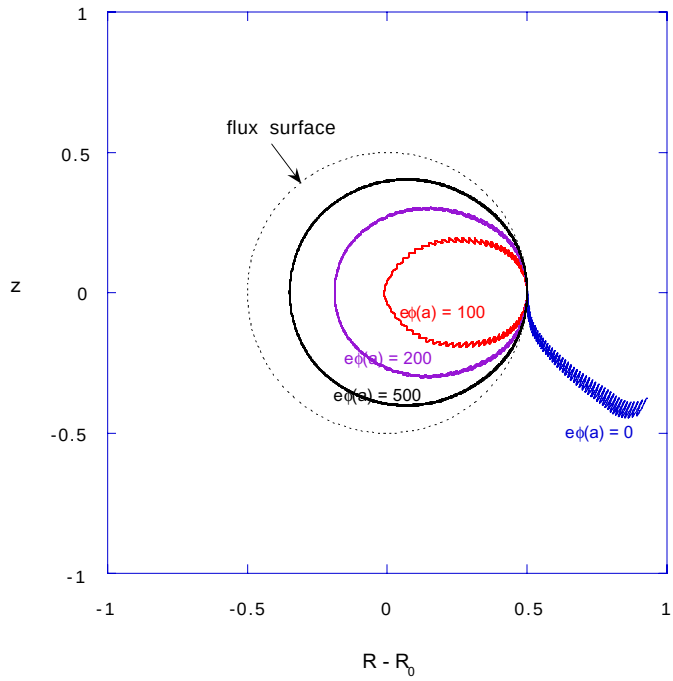

(b)

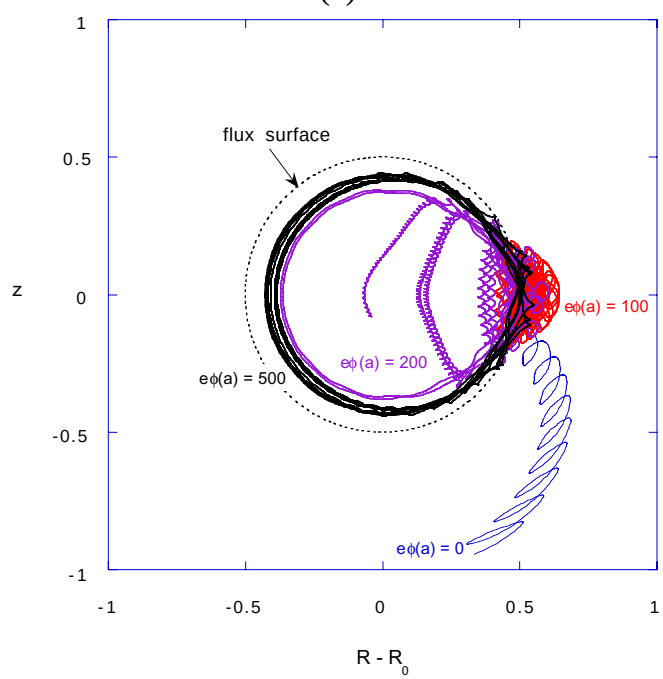

Figure 6.14 - Deeply trapped 500 eV orbits in QPS reference configuration, (b) deeply trapped 500 eV orbits in ATF.

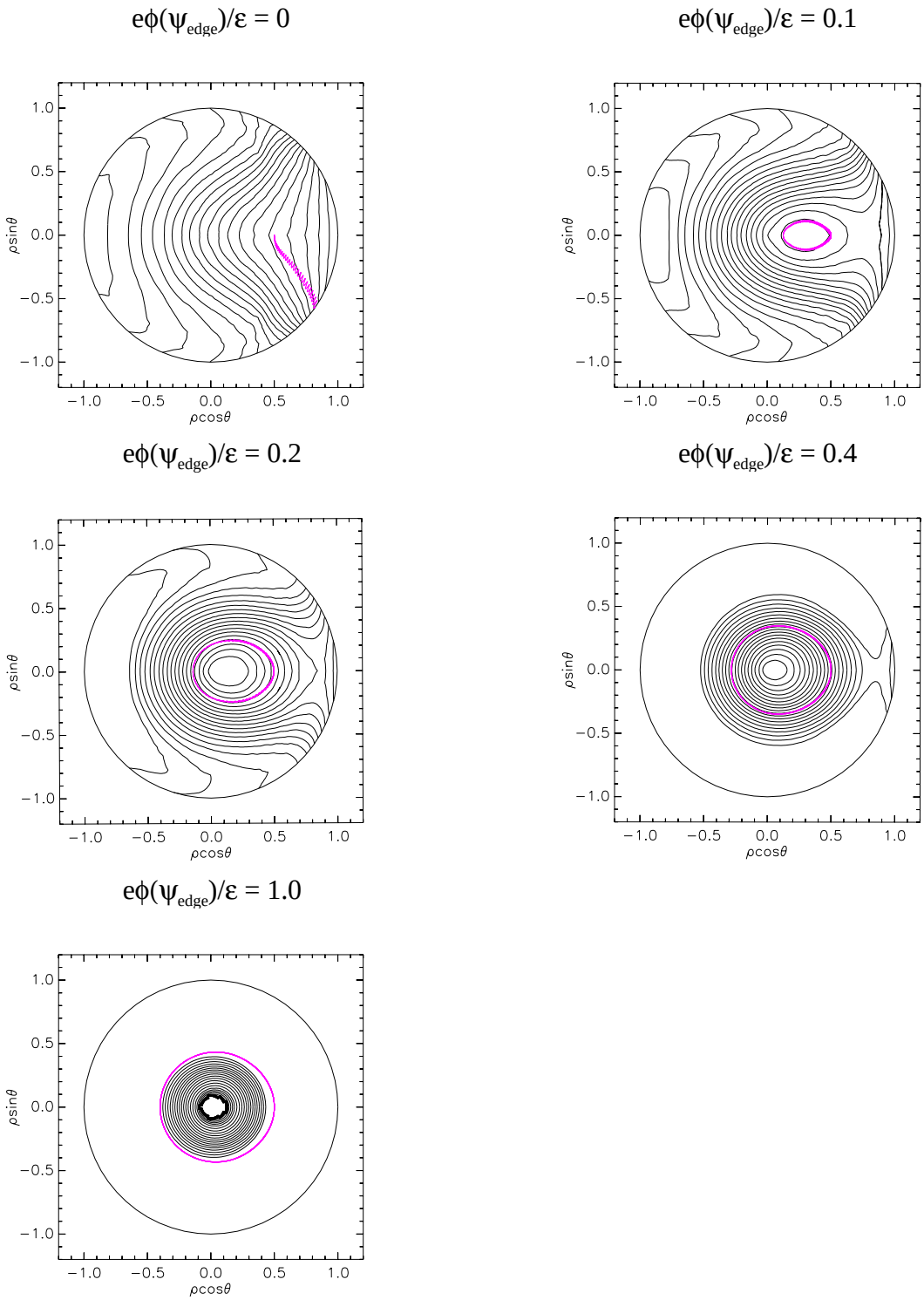

Figure 6.15 - J* contours as a function of ambipolar potential with associated orbits (from Figure 6.14) superimposed in magenta.

These trapped orbit trajectories in the reference configuration match rather well with longitudinal adiabatic invariant contours. The reference configuration has been developed with most of the transport weighting on a DKES collisional ($\nu_* \sim 1$) transport coefficient target in order to improve transport in this regime. In Figure 6.15 we plot the contours of the longitudinal adiabatic invariant J* for the reference configuration with the associated orbits of Figure 6.14 superimposed in magenta. As may be seen, the J* contours generally provide a good guide as to where the orbit trajectory goes and show (in a more global way) how the ambipolar potential improves the orbit confinement. The regions of white–space (no contours) in Figure 6.15 are associated with regions (forbidden) which cannot be accessed due to $v_{\|}^2 < 0$ at these locations for the fixed values of ε/μ used in making these plots. For each of the plots in Figure 6.15 we have plotted only J* contours for a the single value of ε/μ that is consistent with the pitch angle ($v_{\|}/v = 0.1$) and potentials used in the orbit calculation.

In Figure 6.16 we display several of the different types of orbits that are formed as the initial pitch angle of the particle is varied (as $v_{\|}/v$ is varied the orbits are started at different flux surfaces so that they don't lie on top of each other). Here 500 eV ions are followed in an electric potential with $e\phi(\psi_{edge}) = 100V$. The $v_{\|}/v = 0.1$, and 0.3 orbits are locally trapped and precessing poloidally due to the **E** x **B** and ∇**B** x **B** drifts. The $v_{\|}/v = 0.5$ orbit is partially passing (near $\theta = 0°$ and 180°)

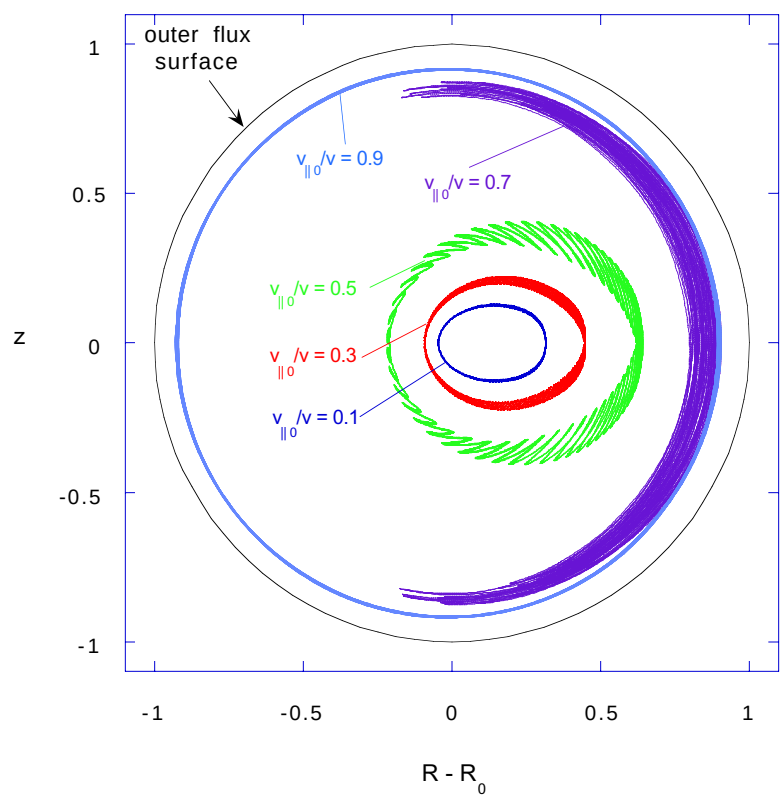

Figure 6.16. Variation of orbit topologies as the initial value of $v_{\|}/v$ and starting flux surface are varied.

and locally trapped over the remaining portions of its trajectory. The $v_{\|}/v = 0.7$ orbit is somewhat similar to a tokamak banana orbit in that it is not locally trapped within a local well in the toroidal direction, but is reflected when it reaches a poloidal position where $v_{\|} = 0$. Finally, the $v_{\|}/v = 0.9$ orbit is untrapped over its entire trajectory. These orbit features are also illustrated in Figure 6.17 where we plot the $v_{\|}/v = 0.3$, 0.5, 0.7, and 0.9 orbits along with their associated J* contours. The color coding used here is that the black contour lines are for the locally trapped orbits (i.e., within a single well of |B| as one moves toroidally); the purple contours are for the untrapped J* contours and the magenta lines denote the guiding center orbit trajectory.

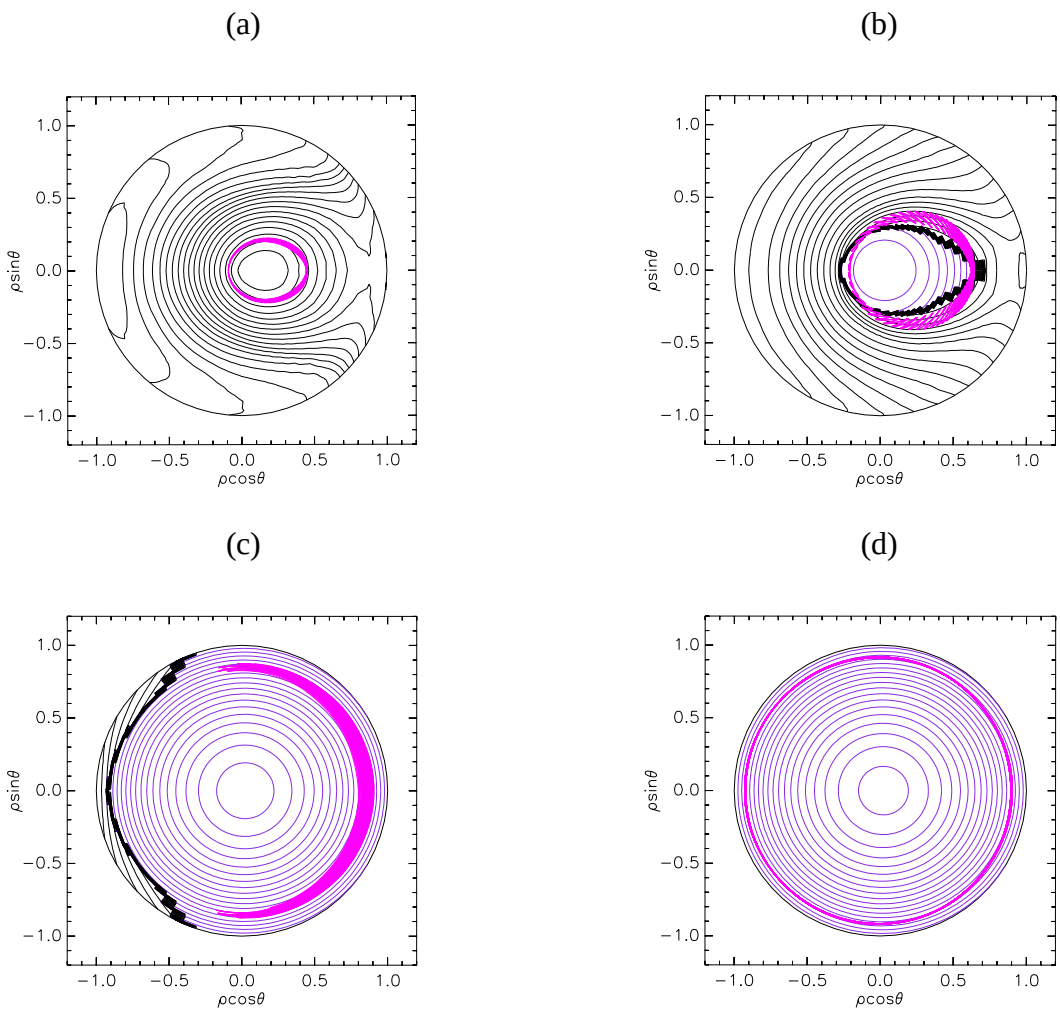

Figure 6.17 Longitudinal adiabatic invariant contours associated with the $v_{\|}/v = 0.3$, 0.5, 0.7, and 0.9 orbits of Figure 6.16. Black contours are for locally trapped orbits, purple contours are for untrapped orbits, and the actual guiding center orbits are displayed in magenta.

The wide range of different orbit topologies possible in these configurations and the finite deviations of certain classes of orbits from flux surfaces (as illustrated in Figure 6.14 and Figure 6.16), has lead us to rely on global Monte Carlo calculations of neoclassical transport(see section 6.3.4). We find, however, that even taking into account such loss channels, the overall loss can generally be maintained at an acceptable level.

6.2.2. Low-collisionality (1/ν) Transport

Recently, a semi-analytic theory[7] and code (NEO) have been developed for evaluating the local diffusion coefficient L11 of the low collisionality 1/ν stellarator transport coefficient (at $E_r = 0$) for arbitrary |B| Fourier spectra. This capability offers a simple and relatively fast method for categorizing levels of low collisionality transport in compact stellarators. This coefficient is proportional to $\varepsilon_{eff}^{3/2}$, where the effective ripple is ε_{eff} . This is computed by matching the value of L11 calculated for an arbitrary |B| spectrum with the analytic form obtained from single helicity calculations. Although this regime (collisionless, no electric field) is somewhat idealized with respect to what is accessed in an experiment, it does provide a useful measure of confinement.

This measure is not currently being used in our optimizations, but may be incorporated into the stellarator optimization code at some point in the future. As will be discussed in the next subsection, low density ECH plasmas in our configuration do access parameters which are fairly deep into the collisionless regime and certainly benefit from minimizing 1/ν type transport.

In Figure 6.18(a) we plot both the effective ripple coefficient $\varepsilon_{eff}^{3/2}$ obtained from the NEO code, the simple helical ripple coefficient $\varepsilon_h^{3/2}$ which is based on measuring the variation of |B| within each flux surface [$\varepsilon_h = (B_{max} - B_{min})/ (B_{max} + B_{min})$], and results for a low collisionality DKES transport coefficient that has been normalized to the NEO results at the $\psi/\psi_{max} = 0.122$ flux surface. As can be seen, the results from the NEO code and the DKES code show the same variation across flux surfaces. For the QPS reference configuration, there is roughly an order of magnitude improvement between $\varepsilon_h^{3/2}$ and $\varepsilon_{eff}^{3/2}$. This difference provides a measure of the effect of the transport optimization (i.e., the influence of the quasi-poloidal symmetry). In Figure 6.18(b) the variation of $\varepsilon_{eff}^{3/2}$ is plotted as we artificially improve the quasi-poloidal symmetry of our device by reducing the size of the $m \neq 0$ components of the B_{mn}'s which are used in the NEO calculation. This demonstrates that $\varepsilon_{eff}^{3/2}$ is directly reduced by increasing the degree of quasi-poloidal symmetry.

Next, in Figure 6.19(a) and (b) we plot $\varepsilon_{eff}^{3/2}$ as a function of $(\psi/\psi_{edge})^{1;/2}$ for several different stellarators. In Figure 6.19(a) results are given for both the current reference configuration (labeled gb4) along with several similar two field period configurations that have improved levels of transport (gb5_12a, gb5_12c, gb5_12d). Figure 6.19(b) shows results obtained for a number of existing and planned stellarators in the world fusion program including the gb4 and gb5_12c

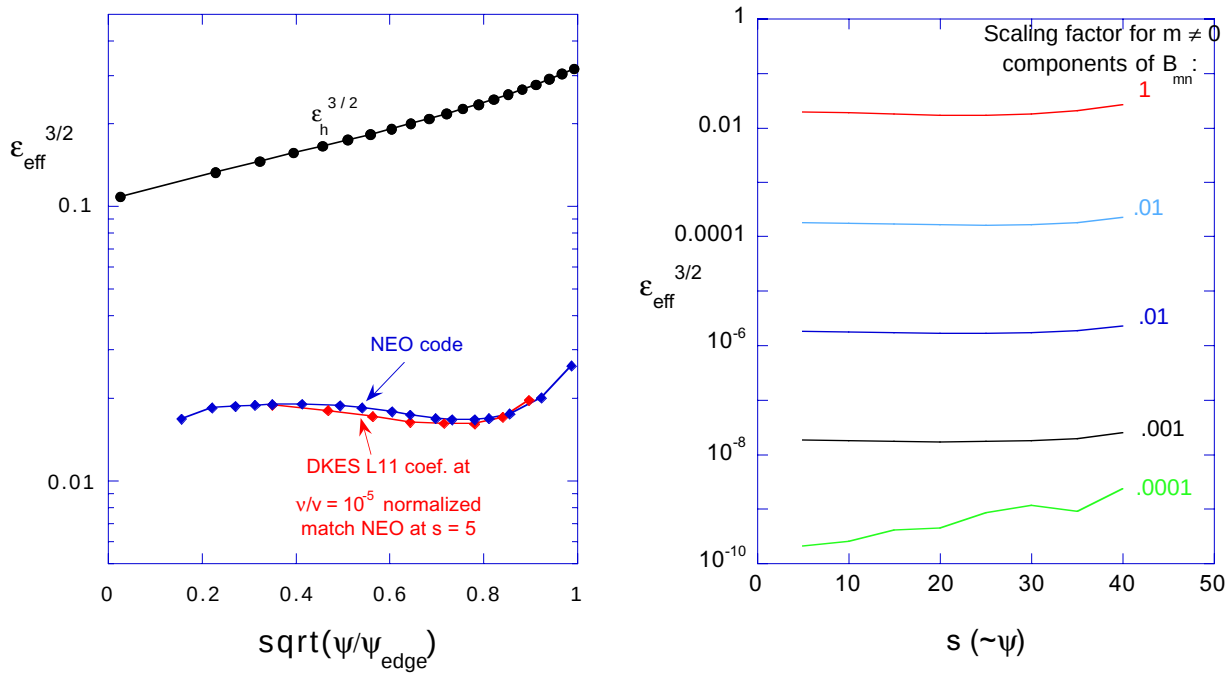

Figure 6.18 - (a) $\varepsilon_h^{3/2}$ and $\varepsilon_{eff}^{3/2}$ for our reference configuration, (b) $\varepsilon_{eff}^{3/2}$ with the components of |B| which violate poloidal symmetry artificially lowered by a constant factor.

QPS configurations. The gb5_12c configuration falls into a similar range of $\varepsilon_{eff}^{3/2}$ as W7-AS. Both gb4 and gb5_12c configurations have values of $\varepsilon_{eff}^{3/2}$ well below those of higher aspect ratio torsatrons (ATF, LHD, CHS) except near the magnetic axis. The quasi-toroidally symmetric LI383 device can attain very low values of $\varepsilon_{eff}^{3/2}$ near the magnetic axis due to the dominance there of n = 0 components in its B_{mn} spectrum and the fact that the axisymmetric ripple vanishes at the axis. It seems to be a characteristic of devices which have a predominantly quasi-poloidal symmetry (our configurations and W7-X) that $\varepsilon_{eff}^{3/2}$ does not drop off as rapidly near the magnetic axis as for quasi-toroidal and quasi-helical devices. Higher aspect ratio devices such as W7-X tend to have less overall ripple and spread in their B_{mn} spectrum, leading to lower levels of $\varepsilon_{eff}^{3/2}$. However, the most highly optimized QPS configuration, gb5_12c, achieves values of $\varepsilon_{eff}^{3/2}$ that fall to within a factor of 2 of W7-X over most of the plasma cross section. This is significant given that this is attained in QPS at an aspect ratio that is a factor of 5 lower than that of W7-X. In comparing the size of $\varepsilon_{eff}^{3/2}$ between devices with different symmetry, it should be noted that $\varepsilon_{eff}^{3/2}$ is only a measure of the low collisionality non-symmetric transport component. The symmetric component of transport must also be added to this. In the case of quasi-poloidal and quasi-helical symmetry this can be quite low as a result of the short toroidal extent and narrow radial thickness of the banana orbits. For quasi-toroidally symmetric devices the symmetric component of transport can be much higher[10] than the ripple component (~ $\varepsilon_{eff}^{3/2}$) computed here.

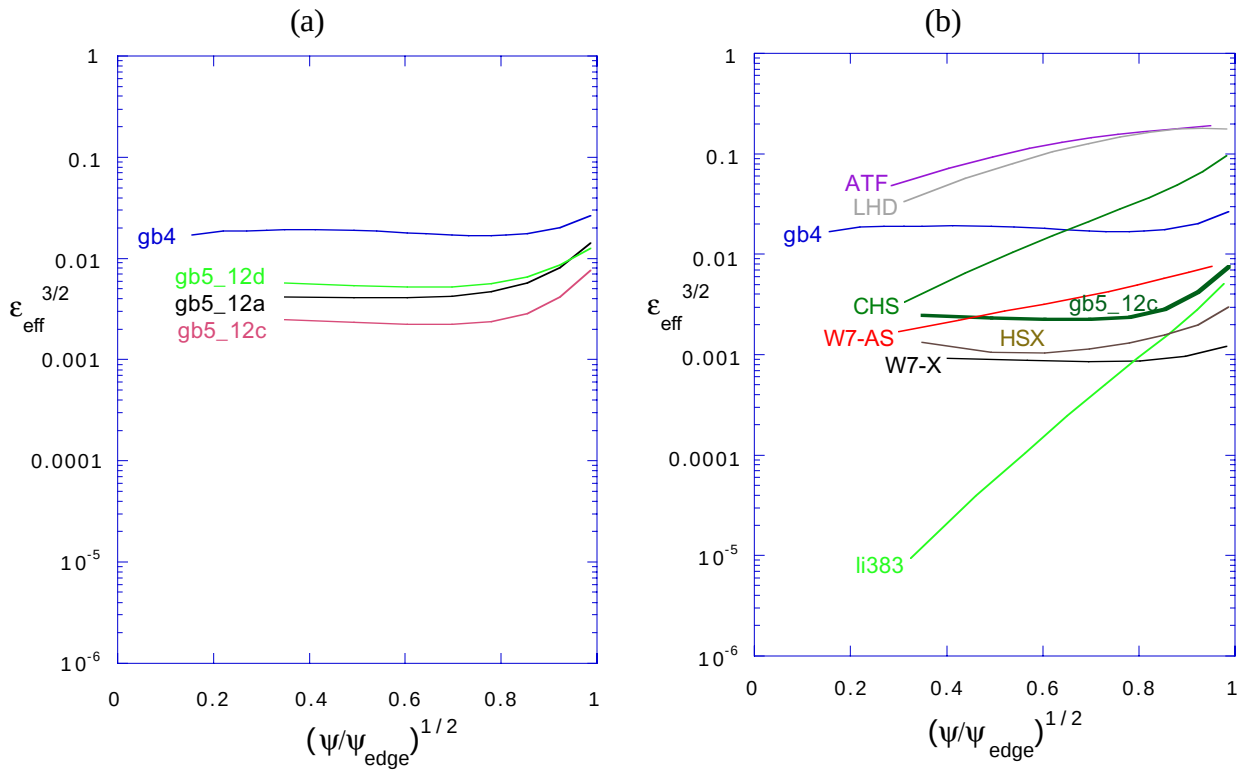

Figure 6.19 - (a) $\varepsilon_{eff}^{3/2}$ coefficient for recent QPS reference configurations, (b) $\varepsilon_{eff}^{3/2}$ coefficient for QPS and various existing and planned stellarator devices.

6.2.3. Neoclassical Transport Coefficient Studies at Arbitrary Collisionality and Electric Field using the DKES Model

The drift kinetic equation solver code (DKES) was developed[11,12] to calculate the full stellarator neoclassical transport coefficient matrix for realistic magnetic field spectra having arbitrary helicities. This code is described in more detail in Appendix A. This code can be used to calculate a variety of the transport characteristics of QPS configurations. These include local transport fluxes of density and heat, global particle and energy lifetimes, collisional bootstrap current levels, and self-consistent calculations of the ambipolar electric field. To date, only some of these options have been developed, but in the future, we expect to use the DKES code and it's projected enhancements to be applied in increasing detail to the confinement analysis of QPS configurations. Limitations of the current DKES model and its anticipated future development are described in Appendix A.

The transport coefficients calculated by DKES relate the radial fluxes of density (Γ), heat (Q) and velocity (u-u_s) to the thermodynamic forces (gradients in density, temperature, and potential in addition to the parallel electric field) that drive them:

$$I_i = \begin{bmatrix} \vec{\Gamma} \bullet \vec{\nabla} s \\ \frac{1}{T} \vec{Q} \bullet \vec{\nabla} s \\ n\left\langle \left(\vec{u} - \vec{u}_s\right) \bullet \vec{B} \right\rangle \end{bmatrix} = -\sum_{j=1}^{3} \hat{D}_{ij} A_j \qquad A_j = \begin{bmatrix} \frac{n'}{n} - \frac{3}{2}\frac{T'}{T} - \frac{eE_r}{T} \\ \frac{T'}{T} \\ -\left(\frac{e}{T}\right)\left(\frac{\langle \vec{E} \bullet \vec{B} \rangle}{\langle B^2 \rangle}\right) \end{bmatrix}$$

The coefficients $\hat{D}_{ij}$ are related to the monoenergetic L_{ij} coefficients that are the output of DKES through the following velocity integrals and dimensional factors:

$$\hat{D}_{ij} = n \frac{2}{\sqrt{\pi}} \int_0^\infty dK \sqrt{K}\ e^{-K} g_i g_j D_{ij}$$

$$\text{where} \quad g_1 = g_3 = 1, \quad g_2 = K, \qquad K = \left(\frac{v}{v_{th}}\right)^2$$

$$D_{11} = D_{12} = D_{21} = D_{22} = -\frac{v_{th}}{2}\left[\frac{Bv_{th}}{\Omega}\left(\frac{d\rho}{dr}\right)^{-1}\right]^2 K\sqrt{K}\ L_{11}$$

$$D_{31} = D_{32} = -D_{13} = -D_{23} = -\frac{v_{th}}{2}\left[\frac{Bv_{th}}{\Omega}\left(\frac{d\rho}{dr}\right)^{-1}\right] K\ L_{31}$$

$$D_{33} = -\frac{v_{th}}{2}\sqrt{K}\ L_{33}$$

Here v_{th} is the thermal velocity, Ω is the cyclotron frequency, K is the energy (normalized to v_{th}^2), B is the flux surface average magnetic field, ρ is the flux surface label, and r is the average minor radius of the ρth flux surface. The reduced monoenergetic transport coefficients L_{ij} are calculated by DKES as a function of two parameters related to collisionality and the local radial electric field: ν/v and E_r/v, where v is the velocity. In order to perform the above velocity integrals, the L_{ij} coefficients must be obtained over a sufficient range of ν/v and E_r/v for each flux surface of interest so that the above integrals can be carried out to a high enough energy so that the $K^n e^{-K}$ factor in the integrand has decayed away sufficiently. For example, in the case of the heat diffusivity coefficient (D_{22}), this factor will be $K^4 e^{-K}$ which typically requires evaluation of L_{11} out to about 9 times the thermal velocity.

DKES has been applied to the reference configurations over the ranges that are currently numerically accessible. Although a sufficient range of collisionalities and electric fields cannot be accessed to do the required energy integrations for all parameters of experimental interest, the monoenergetic coefficients provide useful physical insights over the parameter ranges where they can be converged. Also, a mixed model can be used where the DKES coefficients are employed over the ranges where they can be converged and then asymptotic forms are used to extrapolate outside these ranges. In Figure 6.20 we plot the DKES L_{11} coefficient for a flux surface about 1/2 of the way out (in flux) for our gb4 reference configuration as a function of collisionality and electric field. Also indicated by rectangular boxes are the approximate ranges of collisionality that are accessed in calculating the D_{22} thermal diffusivity coefficient for ECH and ICH parameter regimes at B = 1 T (see Table 6.1). These ranges are estimated as the intervals in ν/v and E/v associated in going from thermal energies to 9 times thermal energies (for D_{22} the integrand has its maximum about halfway through this range). These intervals are: ECH electrons ($7 \times 10^{-5} < n/v < 10^{-3}$, $8 \times 10^{-5} < E/v < 2 \times 10^{-4}$), ECH ions ($6 \times 10^{-3} < n/v < 7 \times 10^{-2}$, $10^{-2} < E/v < 3 \times 10^{-2}$), ICH electrons ($3 \times 10^{-3} < n/v < 4 \times 10^{-2}$, $5 \times 10^{-5} < E/v < 2 \times 10^{-4}$), ICH ions ($2 \times 10^{-3} < n/v < 3 \times 10^{-2}$, $2 \times 10^{-3} < E/v < 6 \times 10^{-3}$).

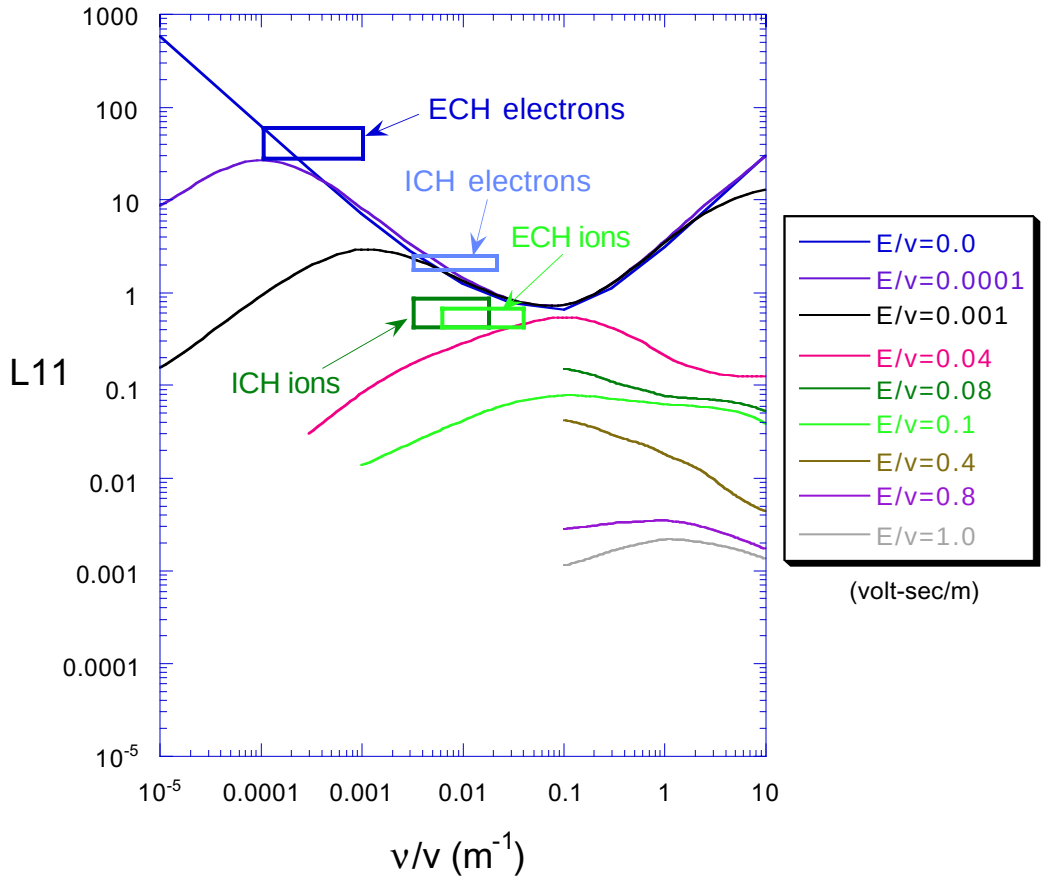

Figure 6.20. Dependence of DKES L_{11} transport coefficients on collisionality and electric field for a single flux surface (halfway out in flux) showing approximate regimes for electrons and ions in ECH and ICH heating scenarios

In Figure 6.21 we plot the L_{31} transport coefficient for the GB4 reference configuration over similar ranges of collisionality and electric field. Bootstrap current profiles can be inferred from this coefficient after extending the calculation to a full range of flux surfaces, integrating over energy and multiplying by pressure gradients. Such a calculation has been carried out to completion for an axisymmetric tokamak, indicating excellent agreement between DKES and low collisionality asymptotic theories.[13] This process has not been completed yet for our reference configuration. As Figure 6.21 shows, it may be expected that the bootstrap current will be suppressed to some extent by finite collisionality and electric field effects.

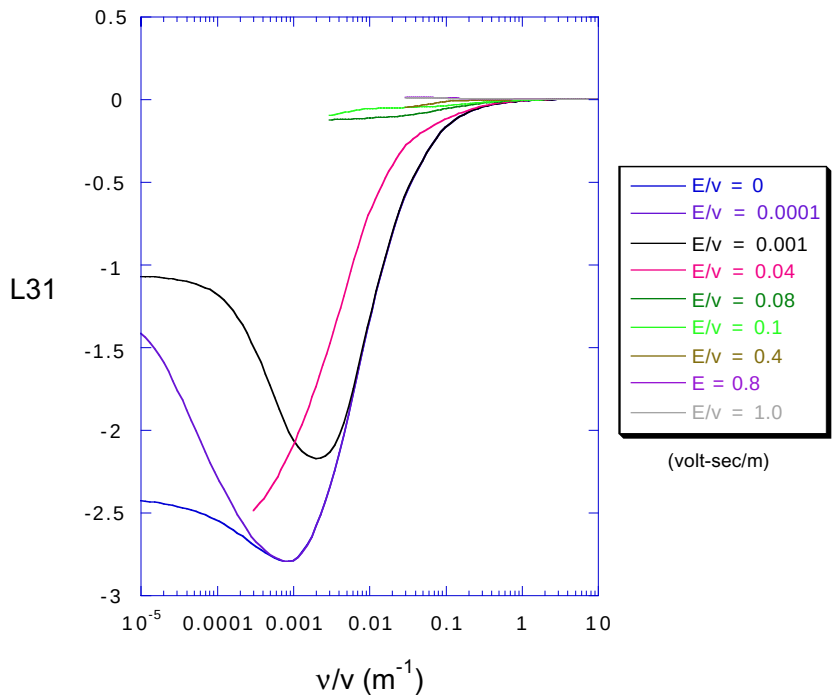

Figure 6.2. Dependence of DKES L_{31} transport coefficients on collisionality and electric field for a single flux surface (halfway out in flux).

We have evaluated DKES transport coefficients at $\psi/\psi_{edge} = 0.5$ and $E/v = 0.0001$ for the gb4 and gb5 series of configurations that were analyzed using the NEO code in Figure 6.19(a). The results are shown in Figure 6.22.

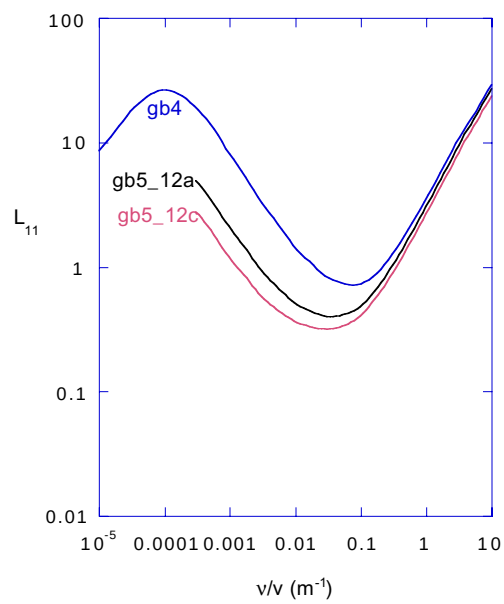

Figure 6.22 - Dependence of DKES L_{11} transport coefficients on collisionality for gb4 and gb5 configurations.

As may be seen, similar improvements are evident in going from gb4 to gb5 configurations as shown by the $\varepsilon^{3/2}$ coefficient (which is a measure of the level of the $1/\nu$ transport regime that occurs in this figure for ν/v < about 0.01).

A final application of DKES in analyzing our configurations is in the calculation of the self–consistent ambipolar electric field; in certain regimes, the level of this field can exert a strong influence over neoclassical confinement times. Also, control of this electric field and its local shear is expected to be a critical element in the achievement of turbulence suppression and enhanced confinement regimes. There are several approaches under consideration for addressing this issue. First, one can use DKES coefficients to calculate ion and electron fluxes and then search for roots. These fluxes can be expressed in terms of the DKES transport coefficients as follows:

$$\Gamma_i = -D_{11}^i(E_r)\left[\frac{n'}{n} - \frac{3}{2}\frac{T'}{T} - \frac{ZeE_r}{T}\right] - D_{12}^i(E_r)\frac{T'}{T}$$

$$\Gamma_e = -D_{11}^e(E_r)\left[\frac{n'}{n} - \frac{3}{2}\frac{T'}{T} + \frac{eE_r}{T}\right] - D_{12}^e(E_r)\frac{T'}{T}$$

In the following Figure 6.23 we give an example of the dependence of these fluxes on the radial electric field using DKES for an earlier reference configuration. As more results become available for the DKES database of current reference configuration, similar calculations will be applied to this device. In this case we have extrapolated the monoenergetic coefficients to asymptotic limits in regimes where it was not possible to obtain converged DKES results. For example, at the lower collisionality, large electric field ranges for calculations such as in Figure 6.20, we have matched over smoothly to a $\nu^{1/2}$ scaling. We have chosen parameters characteristic of the ECH heated regime with $T_e > T_i$. As may be seen the electric field that equalizes electron and ion fluxes is the negative (inward pointing) electron root. As will be shown in the next section, this is qualitatively in agreement with Monte Carlo results for ECH regimes where the overall electric field level has been also varied in order to equalize electron and ion fluxes through the outer flux surface.

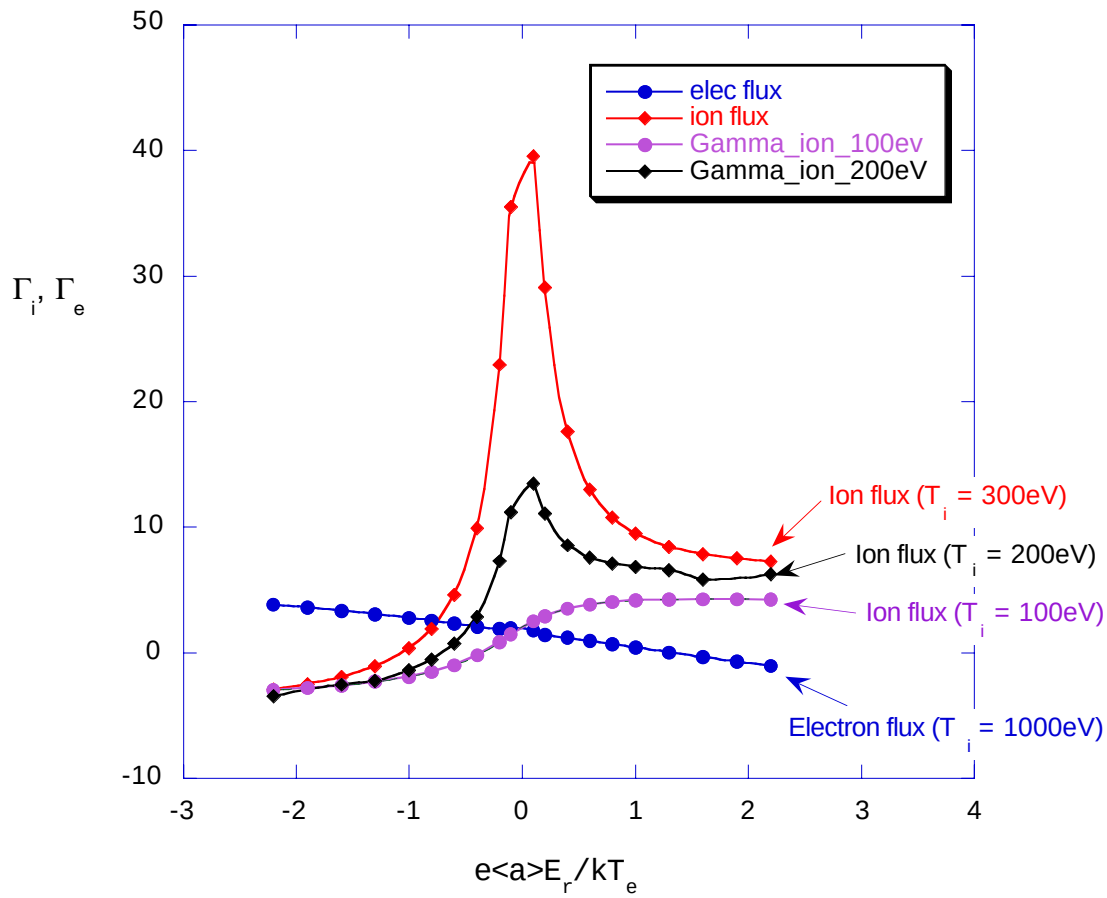

Figure 6.23. Self-consistent ambipolar electric field roots using the DKES transport coefficients for electrons and ions in ECH regimes.

The next step beyond this method of calculating the electric field is to attempt to dynamically balance the ion particle fluxes that are calculated within the Monte Carlo simulation the particle fluxes for electrons obtained from DKES. Such a hybrid diffusive fluid electron – guiding center ion model should avoid the time scale separation problems and noise level problems inherent in using particle models for both electrons and ions.

6.2.3. Monte Carlo Calculations

Global Monte Carlo particle simulations have provided the most frequently used method for estimating global energy lifetimes in QPS configurations. Due to the fact that the full guiding center orbits are followed, this model includes both diffusive and direct orbit losses. Monte Carlo calculations have been based on the DELTA5D code (see Appendix A for a description of this code).

For the evaluation and comparison of different configurations, the global confinement option of DELTA5D based on diffuse profiles has been used most frequently. In this case the initial loading of particles is determined by the assumed density and temperature profiles. We have typically used flat density profiles and parabolic squared temperature profiles. In Figure 6.24(a) we show a

scatter plot of typical initial particle energies vs. flux along with the assumed temperature profile for ~12,000 particles. These particles are initially distributed randomly in poloidal and toroidal angular locations. Their trajectories are integrated in time until they intersect the outer magnetic surface; as they leave this surface their exit energy is added to the accumulated energy loss and they are then re-seeded back into the plasma with random initial conditions and energy chosen from a probability distribution that is consistent with the assumed profiles. In Figure 6.24(b) we show a plot of the typical energy loss rate through the outer magnetic surface, expressed as a percentage fraction of the initial energy. Both the instantaneous signal and the moving time-averaged result is shown, indicating that a steady state is generally achieved where losses are balanced by sources. We typically only use the time-averaged results for energy lifetime predictions.

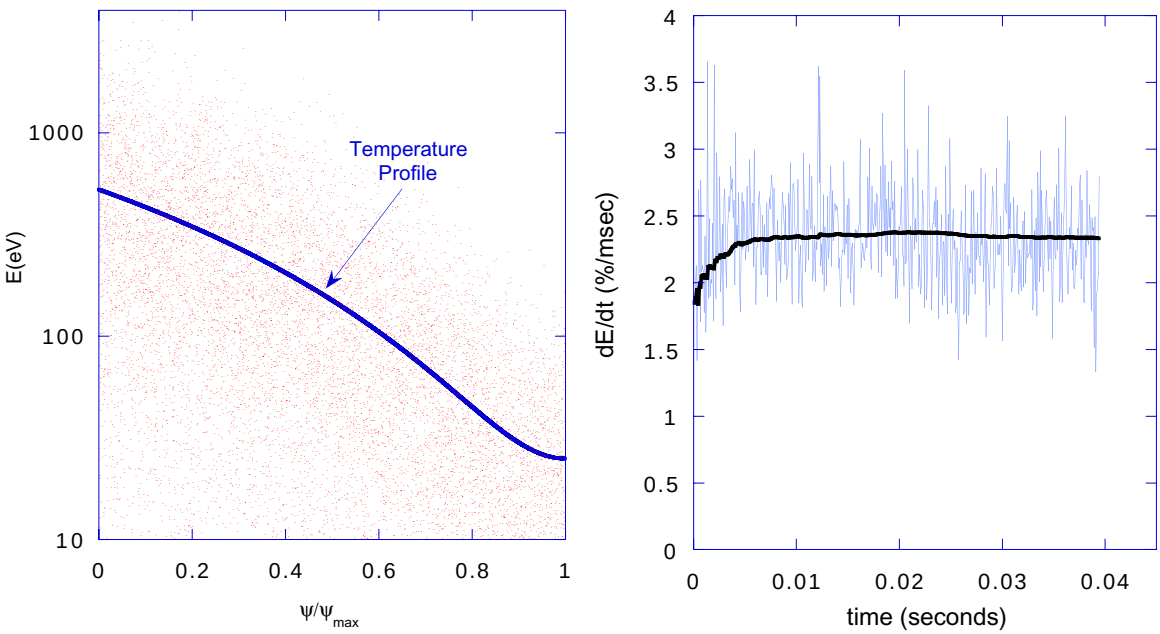

Figure 6.24 - (a) typical Initial Monte Carlo particle loading in energy and radius, (b) Energy loss rate through outer flux surface showing both raw signal (blue) and time-averaged signal (black).

We have generally used a fixed profile for the ambipolar potential that varies inversely with the temperature profiles. An example of typical potential and temperature profiles is shown Figure 6.25.

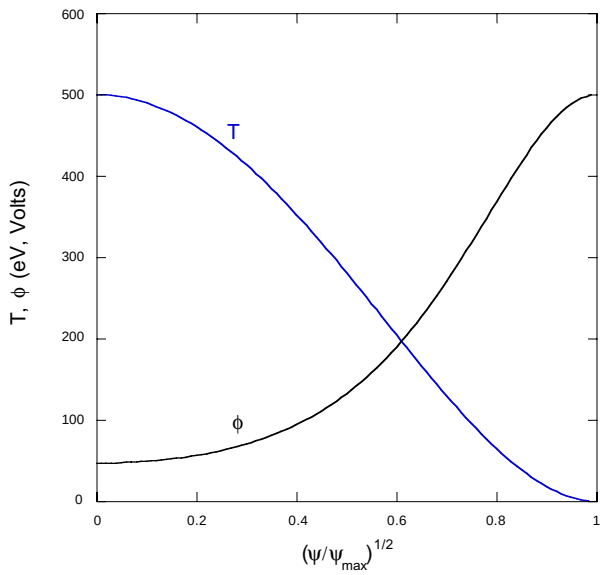

Figure 6.25 - Temperature and ambipolar profiles used in the Monte Carlo calculations.

Keeping this potential profile fixed, we have then varied the central value $\phi(0)$ from negative to positive values to obtain approximate ambipolar states where the electron and ion particle losses through the outer flux surface are balanced.

In following Monte Carlo particle distributions in the presence of an electric potential and for times on the order of collisional energy exchange times, steps must be taken to insure that the average energy of the test particle distribution remains relatively constant in time. If this is not done, then steady-state conditions are not obtained and the definition of a confinement time becomes problematical. Within our model there are a number of mechanisms which can cause changes in the ensemble averaged particle energy over time. These include: energy exchange between the diffusing particles and the fixed background plasma as the initially more energetic particles from near the magnetic axis move radially outward into the cooler portions of the background profile, increases or decreases (i.e., $\pm e\Delta\phi$) in the particle kinetic energy as particles move radially through the potential profile, the effective heating which is built into our particle replacement procedure (as particles leave the outer magnetic surface, they are replaced back at their same initial flux surface at a potential energy of $e\phi$ and a kinetic energy obtained from sampling the local Maxwellian distribution). We find that for the case of ions, especially at high collisionalities, these sources and sinks of energy approximately balance out and no adjustments need to be made. However, for electrons, collisional energy scattering effects generally tend to drain energy out of the test particle distribution over time; if energy scattering is not present, then the opposite trend of kinetic energy gain often occurs due to the radial movement of electrons through an increasing electrostatic potential while conserving their total energy (this feature is built into the guiding center orbit equations). In this case we have adopted a procedure that is similar to that used by Lotz, Nührenberg, and Schlüter[14] which is to keep the kinetic energy of the test particles constant. This is implemented in the current calculations for electrons by including only pitch angle scattering and

resetting the kinetic energy at each time step to its value prior to the time step (i.e., in effect we instantly relax the kinetic energy $\pm e\Delta\phi$ resulting from movement through the varying electric potential). This approach is expected to error in a conservative direction with respect to confinement time estimates in that it doesn't allow the equilibration with the local background plasma (and resulting lower particle energy) which would normally be expected in a more self-consistent calculation. In the future, we expect to explore more self-consistent methods that include collisional energy transfers balanced by local heating allocated over the whole ensemble of simulation particles in order to maintain a steady-state.

Using Monte Carlo calculations we have examined confinement characteristics for the parameters of the <B> = 1 T ECH and ICH cases given above in Table 1. This calculation allows us to examine the dependence on electric field and plasma parameters of both the particle flux through the outer magnetic flux surface and the global energy lifetimes for both electrons and ions. Taking into account the energy loss channels of both species, we can then make direct comparisons to empirical ISS95 energy confinement times.

In Figure 6.26 we plot the particle flux (through the outer flux surface) and the energy confinement time variation with the electric field for the relatively high density, equal electron and ion temperature ICH case from Table 1 [$n(0) = 8.3 \times 10^{19}$ m^{-3}, $T_e(0) = T_i(0) = 0.5$ keV]. As can be seen from Figure 6.26(a), the ion and electron particle fluxes are balanced for an ambipolar electric field with $|e|\phi(\psi_{edge})/kT_e(0) > 0$. This is the ion root, as is often observed in higher density stellarator plasmas. Figure 6.26(b) shows the variation of the energy confinement times with electric field. For the value of the electric field where the global particle fluxes are ambipolar from Figure 6.26(a) the electron energy lifetime is ~210 ms while the ion lifetime is ~315 ms. At $|e|\phi(\psi_{edge})/kT_e(0) = 0$, the electron energy lifetime is ~244 ms while the ion lifetime is ~65 ms. The ion lifetimes rise very steeply for positive values of $|e|\phi(\psi_{edge})/kT_e(0)$. The electron lifetimes remain large and are not strongly dependent on the electric field due to their high collisionality.

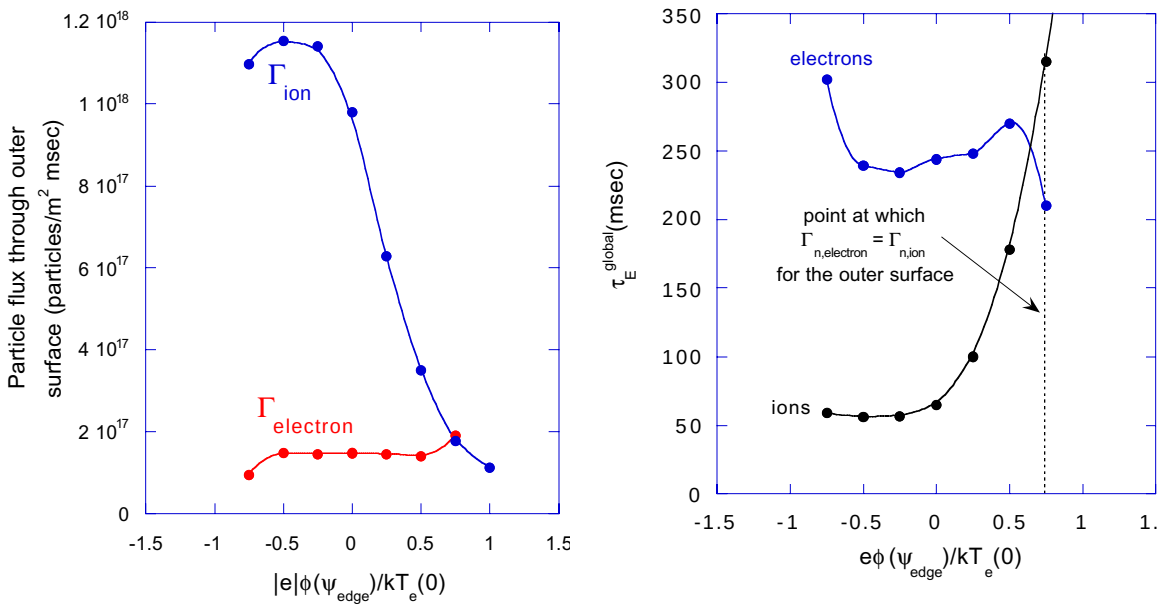

Figure 6.26 - Variation of (a) Edge particle fluxes for ions and electrons vs. electric field for the ICH heated case, and (b) Energy lifetimes for ions and electrons vs. electric field for the ICH heated case.

We can then combine the electron and ion energy loss rates shown in Figure 6.26(b) to obtain a global plasma energy confinement time using the formula:

$$\tau_E^{global} = \frac{\tau_E^i \tau_E^e}{\alpha_e \tau_E^i + \alpha_i \tau_E^e}$$

where $\alpha_i = W_i/(W_i + W_e)$, $\alpha_e = W_e/(W_i + W_e)$, and W_i and W_e are the volume–averaged stored energies in the ions and electrons. Figure 6.27 shows the variation of this global energy confinement time with $|e|\phi(\psi_{edge})/kT_e(0)$ and indicates the level of global confinement time predicted by the ISS95 empirical stellarator scaling law for these parameters.

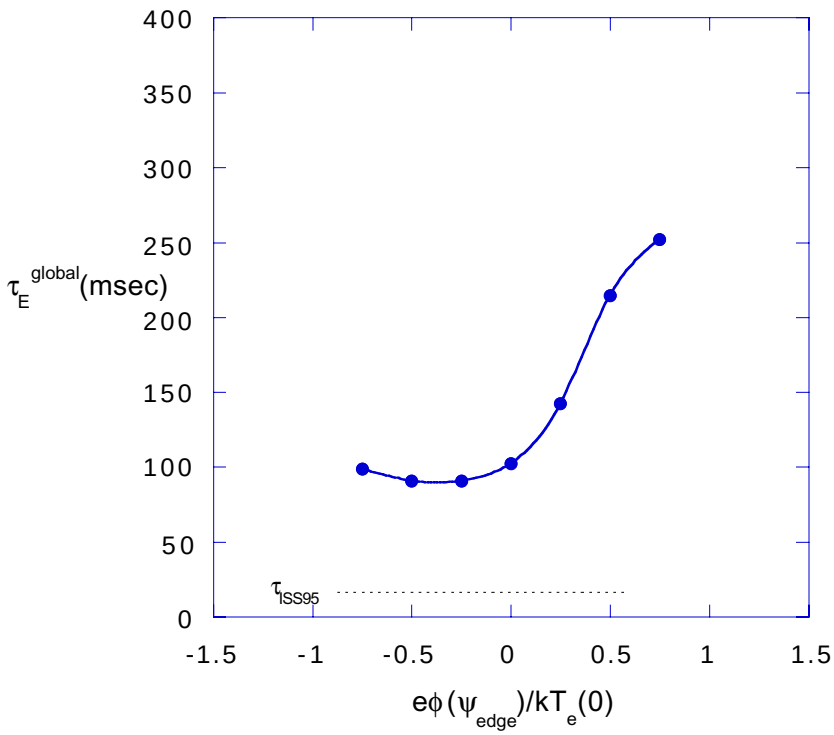

Figure 6.27 - Variation of global neoclassical confinement time from Monte Carlo (in blue) with electric field for ICH heated parameters and comparison with ISS95 empirical stellarator scaling law.

The neoclassical Monte Carlo confinement time exceeds τ_{ISS95} by a factor of 6.3 [for $|e|\phi(\psi_{edge})/kT_e(0) = 0$] to 15 (at the point where the global particle fluxes balance). Clearly, for these parameters, anomalous transport will dominate and neoclassical will limit confinement, except if enhanced confinement regimes are present.

We next used Monte Carlo to analyze the opposite extreme of the spectrum of parameters that should be accessible in the QPS device; i.e., the low density, high electron temperature, low ion temperature ECH case from Table 1 [$n(0) = 1.8 \times 10^{19}$ m^{-3}, $T_e(0) = 1.4$ keV, $T_i(0) = 0.15$ keV]. In Figure 6.28 we plot the electric field variation of the particle flux and the energy confinement times for ions and electrons. As can be seen from Figure 6.28(a), the ion and electron particle fluxes now become balanced for an ambipolar electric field with $|e|\phi(\psi_{edge})/kT_e(0) < 0$. This is the electron root, and is often observed in ECH plasmas with $T_e >> T_i$ where the electrons dominate the transport (reference W7-AS and CHS electron root papers. Figure 6.28(b) then shows the variation of the energy confinement times with electric field. For the point where the particle fluxes are ambipolar from Figure 6.28(a), the electron energy lifetime is ~10 ms while the ion lifetime is ~35 ms. The ion lifetimes rise very steeply for positive values of $|e|\phi(\psi_{edge})/kT_e(0)$ due to the large electron–ion temperature ratio ($T_e/T_i \sim 10$). Since the electric field is electrostatically confining for ions in the $|e|\phi(\psi_{edge})/kT_e(0) > 0$ direction, it is difficult to populate the Maxwellian Monte Carlo ion distribution with enough tail ions to provide sufficient losses to define a confinement time for

$|e|\phi(\psi_{edge})/kT_e(0)$ in the 0.25 - 1 range [equivalent to $|e|\phi(\psi_{edge})/kT_i(0) = 2.5 - 10$]. On the other hand, ion lifetimes monotonically decrease as $|e|\phi(\psi_{edge})/kT_e(0)$ varies from 0 to -2. For this sign of the potential, tail ions are not restrained electrostatically and due to the large electron-ion temperature ratio these electric fields can drive sufficiently large **E** x **B** drifts in the low temperature ions so as to begin unwinding their rotational transform; this effect can enhance losses for localized groups of passing ions with energies and pitch angles such that the poloidal component of their parallel motion along the field lines matches their poloidal **E** x **B** drift.

The electron root is of interest with respect to enhanced confinement regimes since it can lead to large potentials and electric field shear and improved ion confinement. It is expected that higher electron temperatures would increase the electron particle flux in Figure 6.28(a), leading to a larger ambipolar electric field. Figure 6.28(b) indicates that for the range of $|e|\phi(\psi_{edge})/kT_e(0)$ which has been simulated, the ion confinement is decreasing with increasingly negative values of $|e|\phi(\psi_{edge})/kT_e(0)$. However, it would be expected that as one moves further to the left on Figure 6.28(b) than has been simulated, the ion confinement will again begin increasing at some point.

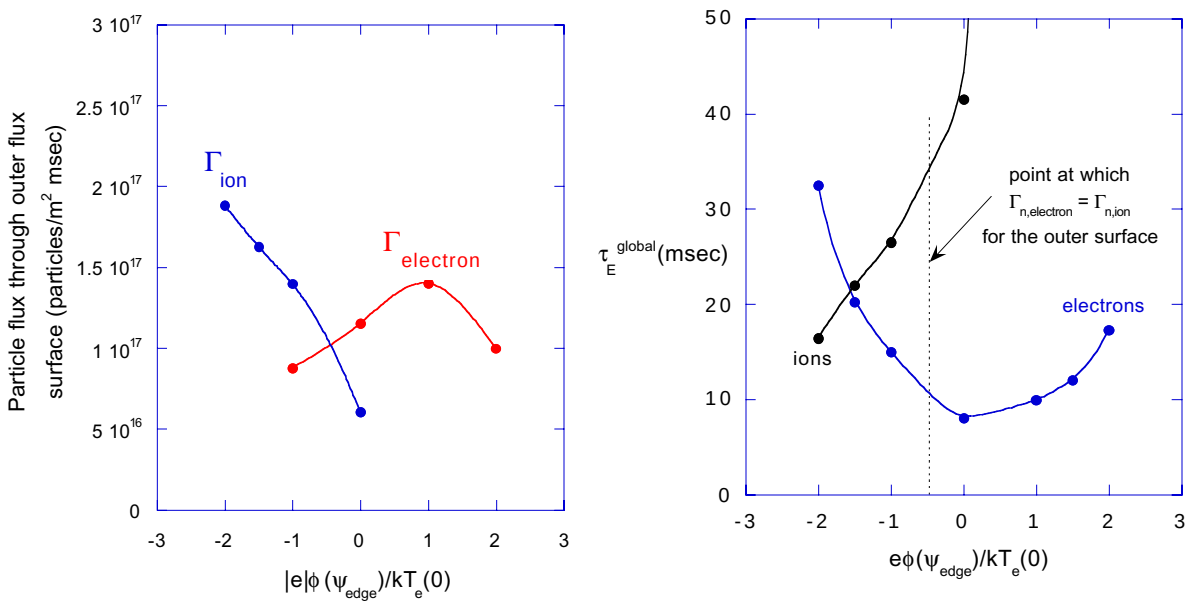

Figure 6.28. Variation of (a) Edge particle fluxes for ions and electrons vs. electric field for the ECH heated case, and (b) Energy lifetimes for ions and electrons vs. electric field for the ECH heated case.

Using the above formula for the overall global lifetime and the results from Figure 6.28(b), we plot in Figure 6.29 the variation of the global energy confinement time with $|e|\phi(\psi_{edge})/kT_e(0)$ and indicate the level of global confinement time predicted by the ISS95 empirical stellarator scaling law for these parameters.

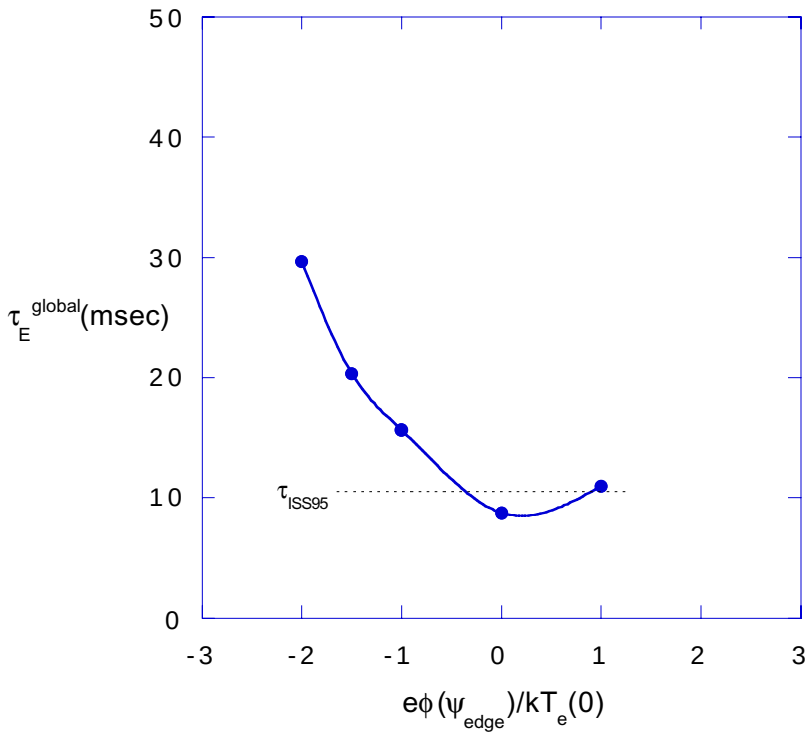

Figure 6.29. Variation of global neoclassical confinement time from Monte Carlo (in blue) with electric field for ECH heated parameters and comparison with ISS95 empirical stellarator scaling law.

In contrast to the ICH case, here the neoclassical lifetime is comparable to the anomalous ISS95 lifetime. Based on this prediction, both types of transport should be present at roughly equal levels. This lowered level of neoclassical confinement for the ECH as compared to ICH parameters reflects the lower collisionality, in particular for the electrons in the ECH case and their sampling of the $1/\nu$ regime of transport, as was indicated in Figure 6.20.

Next, in Figure 6.30 we compare Monte Carlo energy confinement times between the QPS gb4 reference configuration (gb4) and the ATF torsatron for ECH and ICH parameters. This is based on the full-size ATF and shows roughly a factor of 2 improvement in confinement in each case.

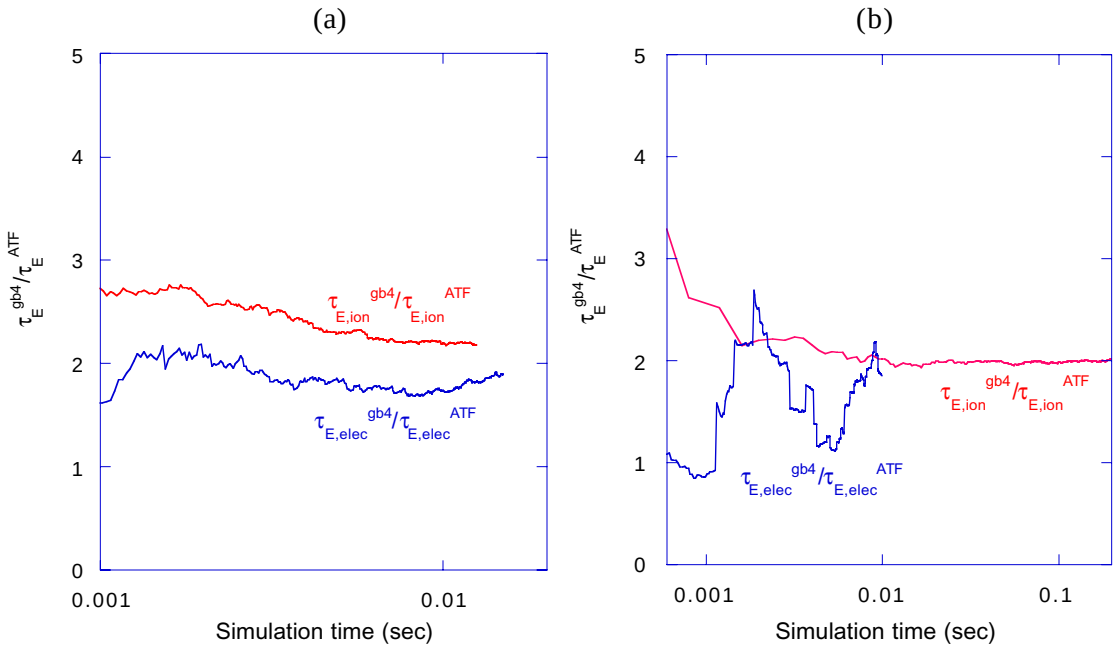

Figure 6.30 - Comparison of energy lifetimes between the QPS reference configuration (gb4) and the ATF torsatron at $|e|\phi(\psi_{edge})/kT_e(0) = 0$ for (a) ECH parameters and (b) ICH parameters.

As mentioned earlier, improvements have recently been made over the gb4 reference configuration with respect to transport optimization. These configurations have been denoted the gb5_12a, . . . gb5_12d series. We have picked the gb5_12a configuration to compare with the gb4 device using an equivalent set of Monte Carlo runs for electrons and ions in ECH and ICH heating scenarios. Based on the low collisionality DKES and $\varepsilon_{eff}^{3/2}$ results, the gb5_12a transport coefficients were about a factor of 4 – 5 lower than those of the gb4 configuration.

In Figure 6.31 we compare the energy lifetimes for the gb4 and gb5_12a configurations for ICH parameters. The ion energy lifetime is improved for the gb5_12a device, but the electron energy lifetime is somewhat lower. These differences are likely within the inherent noise level of the Monte Carlo simulation. However, since the losses are dominated by the ion channel, the global energy lifetime, shown in Figure 6.32, is higher for the gb5 device (the equivalent gb4 result was shown in Figure 6.27) and indicates a factor of 7 – 8 improvement over the ISS95 prediction.

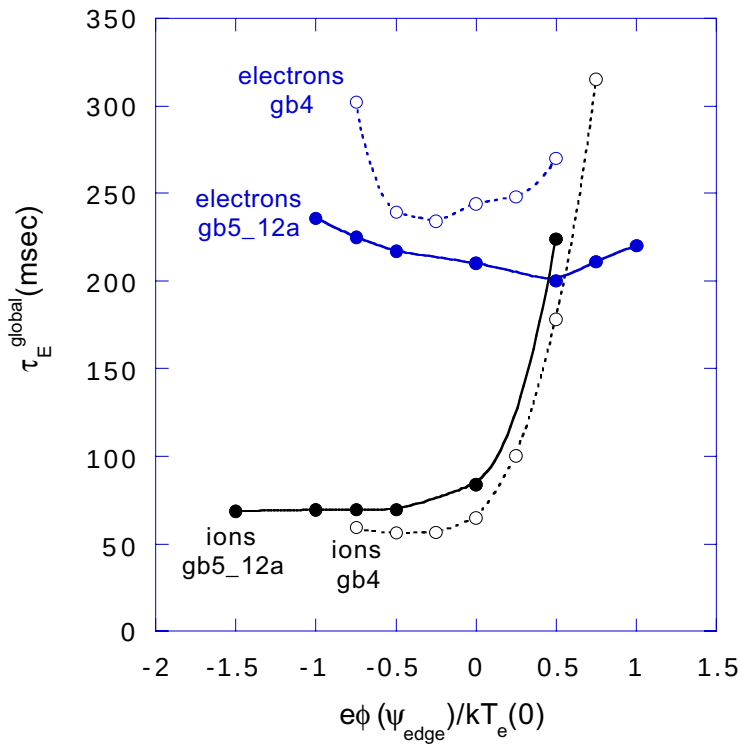

Figure 6.31 - Comparison of electron and ion energy lifetimes vs. electric field between the gb4 and gb5 configurations for the ICH heating parameters.

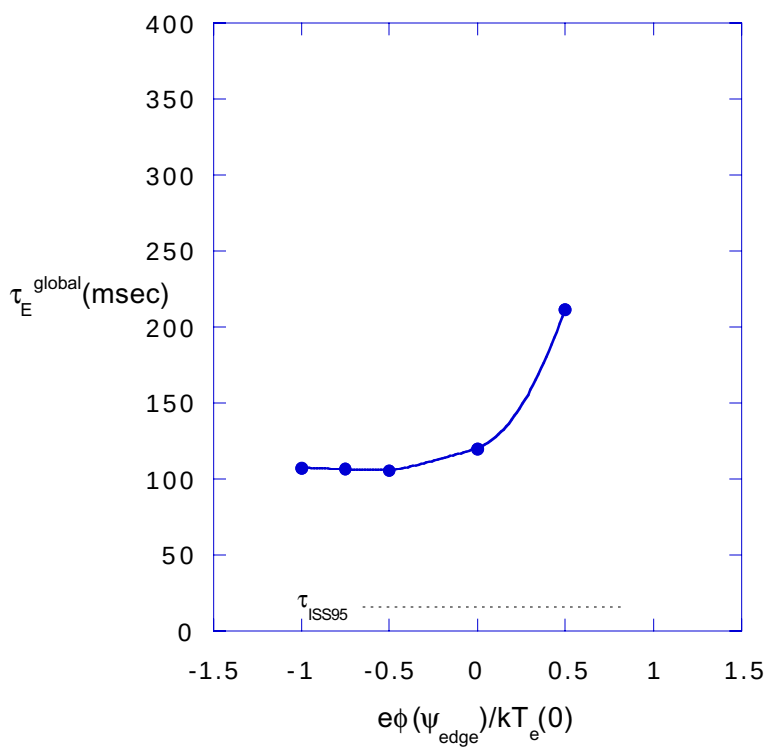

Figure 6.32 - Comparison of global neoclassical energy lifetime vs. electric field for the gb5 configuration with the ISS95 lifetime for the ICH heating parameters.

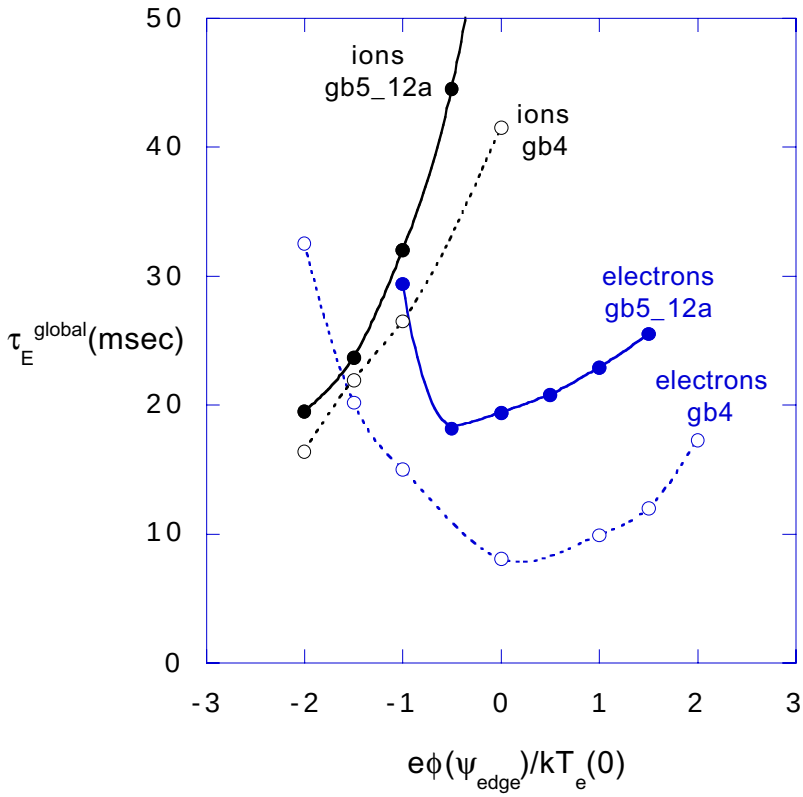

Figure 6.33 - Comparison of electron and ion energy lifetimes vs. electric field between the gb4 and gb5 configurations for the ECH heating parameters

In Figure 6.32 results for gb4 and gb5_12a configurations are compared for the ECH heating scenario. Here more significant confinement time improvements are obtained for the gb5_12a device, especially for the electrons. Since the electrons are well into the collisionless $1/\nu$ regime, it would be expected that their confinement would be more sensitive to configuration optimizations that improve $\varepsilon_{eff}^{3/2}$. For these parameters, the energy losses are generally dominated by electrons. The global confinement time is plotted in Figure 6.34 and compared with the ISS95 scaling result. Significant improvements are evident over the gb4 results of Figure 6.29. Previously (gb4), the global Monte Carlo confinement time was approximately equal to the ISS95 time. With the improved gb5_12a configuration the global Monte Carlo confinement time now exceeds the ISS95 result by a factor of ~2.

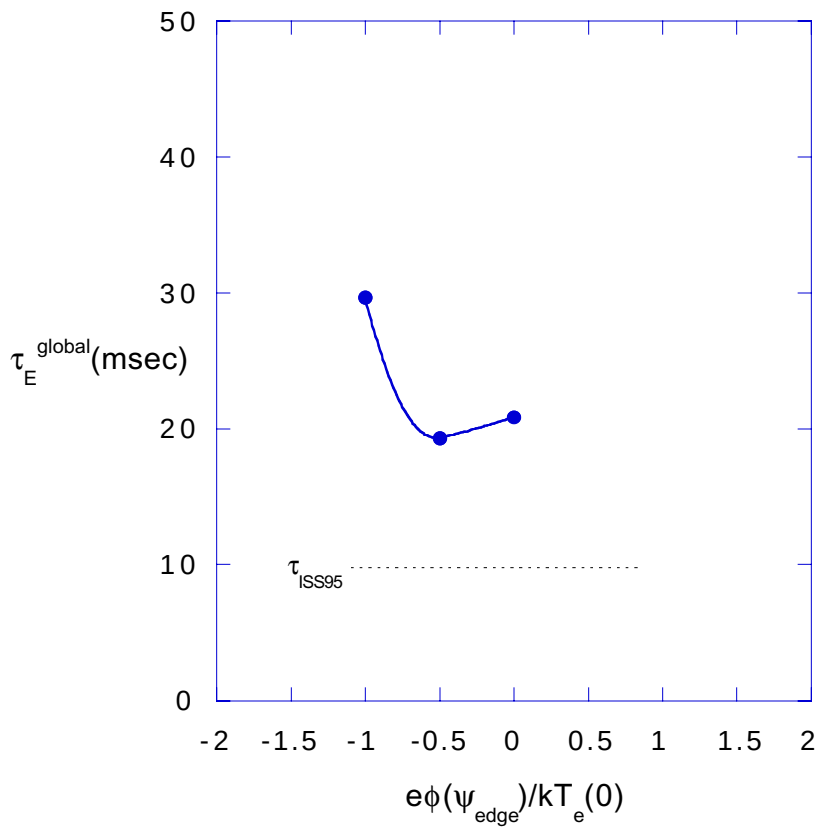

Figure 6.34 - Comparison of global neoclassical energy lifetime vs. electric field for the gb5 configuration with the ISS95 lifetime for the ECH heating parameters.

6.2.4. Comparisons of Transport between Fixed and Free Boundary Configurations

An important test of the modular coil design for our reference configuration is to check that one can reconstruct the original physics properties of the configuration using the free boundary equilibrium obtained from discrete coils. We have checked this issue with respect to transport properties by: (a) using the NEO code to calculate $\varepsilon_{eff}^{3/2}$, and (b) calculating Monte Carlo energy lifetimes for fixed and free boundary configurations.

Results for $\varepsilon_{eff}^{3/2}$ are shown below in Figure 6.34 for fixed and free boundary configurations.

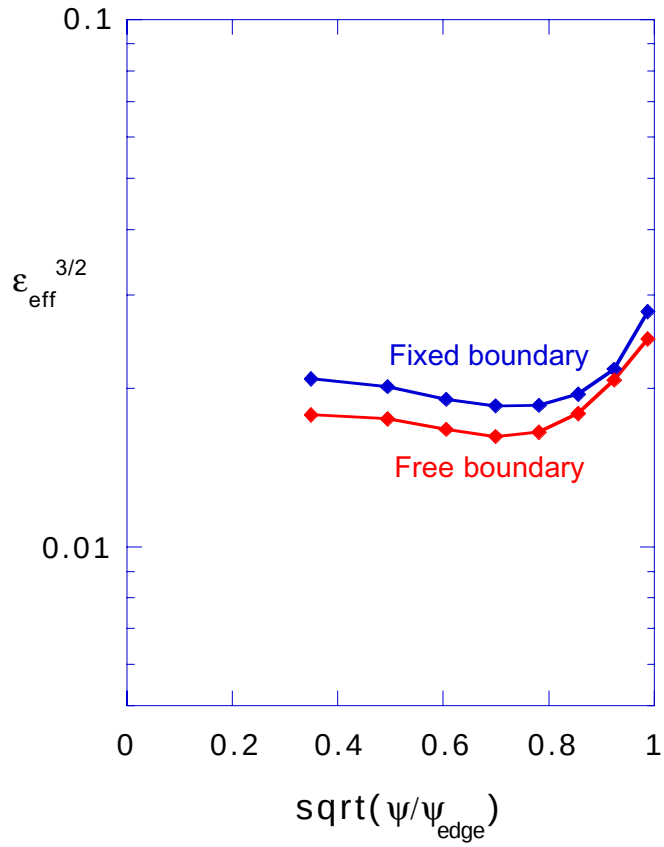

Figure 6.34 - $\varepsilon_{eff}^{3/2}$ vs. flux surface label as obtained from the NEO code for fixed and free boundary (based on the gb4 modular coil design) equilibria.

It is interesting that based on this measure, the free boundary configuration actually improves confinement slightly in going from the fixed to free boundary configurations.

In Figure 6.35 Monte Carlo energy lifetimes are shown vs. simulation time for ions and electrons for the ICH regime parameters [i.e., $n(0) = 8.3 \times 10^{19}$ m^{-3}, $T_e(0) = T_i(0) = 500$ eV]. Here we have calculated lifetimes for $E_r = 0$.

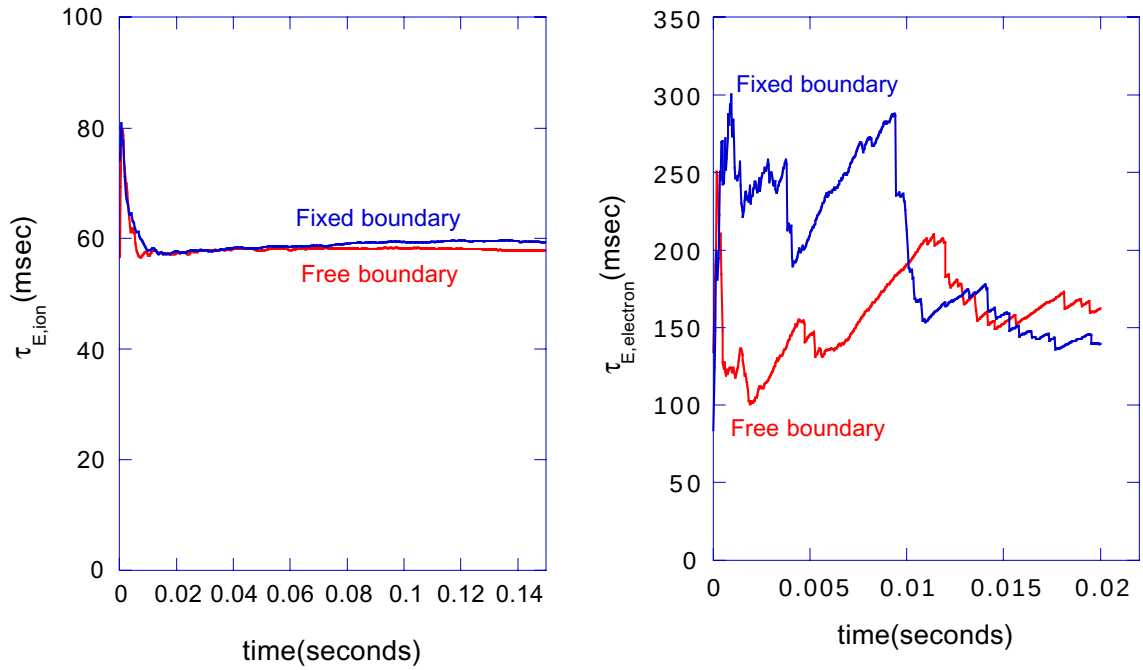

Figure 6.35 - (a) Ion energy lifetimes and (b) electron energy lifetimes vs. simulation time for fixed and free boundary (based on the gb4 modular coil design) equilibria.

As may be seen, the ion energy lifetimes [Figure 6.35(a)] are quite close between the fixed and free boundary configurations with the fixed boundary confinement being slightly higher. For the electron simulations [Figure 6.35(b)], there seems to be a tendency in the opposite direction - i.e., for the free boundary case to have slightly higher confinement times (after the initial transients) than the fixed boundary case. The electron lifetimes show more dispersion, but this is largely due to the larger noise levels that characterize electron simulations. These larger noise levels are related to: (a) the shorter time steps required for the higher electron velocity and collisionality prevent using as many particles as for ions, (b) the higher lifetimes for electrons imply a smaller sample size of escaping particles (used to compute the global lifetimes), and finally, due to the higher computational requirements of following electrons, it is difficult to run the simulation for longer than a fraction of the energy confinement time.

In conclusion, these tests show that the reconstructed free boundary equilibrium based on modular coils preserves the transport properties of the reference configuration both in the collisionless ($1/\nu$) regime (based on the $\varepsilon_{eff}^{3/2}$ coefficient of the NEO code) and for the more collisonal ICH regime (based on Monte Carlo calculations).

References

[1] D. A. Spong, S. P. Hirshman, et al., Plasma Physics Reports **23**, 483 (1997).

[2] S. P. Hirshman, D. A. Spong, Phys. Rev. Lett., **80**, 528 (1998).

[3] D. A. Spong, S. P. Hirshman, et al., Phys. Plasmas, **5**, 1752 1998).
[4] D. A. Spong, S. P. Hirshman, et al., Nuclear Fusion 40, 563 (2000).
[5] S. P. Hirshman, D. A. Spong, et al., Phys. Plasmas, 6, 1858 (1999).
[6] J. A. Rome, Nuclear Fusion **35** (195) 1995.
[7] V. V. Nemov, S. V. Kasilov, W. Kernbichler, M. F. Heyn, Phys. Plasmas **6**, 4622 (1999).
[8] D. A. Spong, J. Carlsson, D. B. Batchelor, et al., Bull. Am. Phys. Soc. **44**, 215 (1999).
[9] Z. Lin, et al., Phys. Plasmas **2**, 2975 (1995).
[10] NCSX Physics Validation Review, March, 2000.
[11] W. I. van Rij, S. P. Hirshman, Phys. Fluids B, **1** (March, 1989).
[12] S. P. Hirshman, K. C. Shaing, et al., Phys. Fluids, **29** (September, 1986).
[13] K. C. Shaing, E. C. Crume, et al., Phys. Fluids, **B1**, 148 (1989).
[14] W. Lotz, J. Nührenberg, and A. Schlüter, Journal of Computational Physics **73**, 73-84 (1987).